Geophys. J. R. astr. Soc. (1982) **70**, 435–485

Viscous gravitational relaxation

Patrick Wu and W. R. Peltier *Department of Physics, University of Toronto, Toronto, Ontario M5S 1A7, Canada*

Received 1982 January 12; in original form 1981 July 30

Summary. This paper is concerned with a detailed examination of the response of Maxwell models of the planet to surface mass loads. Particular attention is devoted to an examination of the factors which determine the isostatic response since the understanding of this response is crucial in a number of different geodynamic problems. One particular example which we discuss in detail is concerned with the prediction of free air gravity anomalies produced by large-scale deglaciation events. Using the methods developed here we are able to provide the first direct assessment of the importance of initial isostatic disequilibrium on the observed relative sea-level variations and free air gravity anomalies forced by the melting of the Laurentide ice sheet. We are therefore able to estimate the extent to which such initial disequilibrium might influence the inference of mantle viscosity from isostatic adjustment data. Our calculations establish that free air gravity data, although they are sensitive to the degree of initial disequilibrium, provide an extremely high quality constraint upon the viscosity of the lower mantle.

1 Introduction

The inference of mantle viscosity from the study of slow, deglaciation-induced changes in the Earth's shape is a geodynamic problem on which active work has continued for approximately fifty years. The earliest efforts by Haskell (1935) and others were based upon Newtonian viscous half-space models of the planet and showed that an instantaneously applied and spatially periodic normal stress on the free surface relaxed exponentially in time. The relaxation time constant for a model with constant density and viscosity was shown to be proportional to the product of the viscosity of the mantle and the wavenumber of the applied load. McConnell (1965), motivated by Crittenden's (1963) work on the uplift of Pleistocene Lake Bonneville, extended Haskell's half-space analysis to allow both for a depth dependence of viscosity and for the effect on the response of the high viscosity surface lithosphere. In McConnell's model, which was applied to interpret the relaxation data from Fennoscandia, the temporal decay of a harmonic surface deformation was still governed by a single characteristic decay time.

Beginning in the early 1970s, new isostatic adjustment data became available from the response of North America to the melting of the Laurentide ice sheet which covered all of Canada and parts of the north-eastern United States. Walcott (1970) reported some evidence in the new data for slight variations of apparent relaxation time with time from specific relative sea-level curves. The existence of this new data set concerning the relaxation of a surface depression of much larger spatial scale than that of Fennoscandia promised the possibility of considerable improvement in the ability to resolve the variation of mantle viscosity with depth. Parsons (1972) showed that the information content in the Fennoscandia data was such that the relaxation carried no information on mantle viscosity from depths in excess of about 600 km. The Laurentide data appeared to offer equivalent information from depths in excess of three times this, a crucial contribution given that convection theorists at the time were relying on a sharp increase of viscosity across the seismic discontinuity at 670 km depth in order to restrict convection to the upper mantle.

Interpretation of the data from the Laurentide region clearly required a global model of the adjustment process and such models were fairly rapidly forthcoming. Parsons (1972) constructed a Newtonian viscous spherical model which he used to investigate the dependence of relaxation time upon wavelength in a viscosity and density stratified sphere. These calculations demonstrated that discontinuities in density in the interior of such an earth model lead to additional relaxation times for fixed spherical harmonic wavenumber. Cathles (1975) constructed a spherical model of the rebound process which also included the elastic response to unloading and used it to predict relative sea-level histories at several sites near the Laurentide and Fennoscandian ice sheets. His model neglected viscoelastic coupling, however, and was implemented by separately integrating different sets of field equations for the elastic and viscous components of the response. Peltier (1974, 1976) employed correspondence principle methods to show that a complete viscoelastic theory of the adjustment process could be obtained using a normal mode formalism. The structure of this theory was such that it integrated all previous work and included important physical effects, such as elastic-viscous coupling, which had previously been omitted. It also proved possible, using a Greens function for the system synthesized in terms of normal modes, to make relative sea-level predictions in which the self-gravitation of the oceans was properly accounted for (Clark, Farrell & Peltier 1978; Peltier, Farrell & Clark 1978). A recent review of work completed using this theory will be found in Peltier (1981) and new extensions of the analyses are discussed in Wu & Peltier (1982).

This paper is concerned with further elaborations of the basis theoretical structure which were necessary in order that the model might be tested against geophysical observables other than relative sea-level histories. Although our interest was initially confined to free air gravity data, we found that the same new analysis was required in order to use the model to make predictions of deglaciation-induced stress in the mantle and to understand the extent to which the continuous glaciation-deglaciation cycle of the ice age might induce real wander of the Earth's rotation pole relative to the surface geography (Sabadini & Peltier 1981). In order to understand each of these phenomena we must be able to calculate the final state of isostatic equilibrium which is achieved in the limit of infinite time when the planet is loaded by the addition to its surface of a point mass. The necessity of this is clear in the case of free air gravity data since these data are a direct measure of the current extent of isostatic disequilibrium. Unless we can predict the infinite time response we will clearly not be able to predict the instantaneous deviation from it.

As well as providing a complete discussion of the infinite time response of the system, to which we shall refer as the 'isostatic response', the following sections will also provide some elaboration of important details of the viscoelastic calculation which have not previously

been described at length. Among these are: (1) direct assessment of the importance of elastic-viscous coupling; (2) a discussion of the crucial impact of this coupling on the dynamics of models with lithospheres; (3) an assessment of the importance of the assumption of initial isostatic equilibrium in the interpretation of relative sea-level and free air gravity data; and (4) an attempt to fit present-day free air gravity anomalies with simple disc load disintegration models of the main Pleistocene ice sheets. We will begin with a brief elaboration of the theoretical structure itself.

2 The viscoelastic field theory

The constitutive relation which has been employed in our past analyses of glacial isostatic adjustment, and which we shall continue to employ here, is that for a Maxwell solid. When it is subject to an applied shear stress such material initially behaves as a Hookean solid but 'finally' as a Newtonian viscous fluid. Although this constitutive relation cannot provide a complete description of the viscoelasticity of the mantle, since it does not include the transient anelasticity necessary to explain seismic Q, it nevertheless suffices for the analysis of isostatic adjustment. This is because of the relatively low value of the elastic defect and of the relatively short time-scale over which the shear modulus relaxes (Peltier, Wu & Yuen 1981). The stress–strain relation of the Maxwell solid is linear and as such violates laboratory data on the steady state creep of olivine single crystals (Kohlstedt & Goetze 1974). It is becoming increasingly evident, however, that polycrystalline materials at the relatively low stress levels typical of mantle convection and post-glacial rebound behave in a much more Newtonian fashion since deformation may then be controlled by grain boundary processes such as superplasticity (Twiss 1976; Berckhemer, Auer & Drisler 1979). We therefore continue to use the linear Maxwell constitutive relation in the form (Peltier 1974)

$$\dot{\tau}_{kl} + \frac{\mu}{\nu}\left(\tau_{kl} - \frac{1}{3}\tau_{kk}\delta_{kl}\right) = 2\mu\dot{e}_{kl} + \lambda\dot{e}_{kk}\delta_{kl} \tag{1}$$

where τ_{kl} and e_{kl} are respectively the stress and strain tensors, the dot denotes time differentiation, δ_{kl} is the unit diagonal tensor, λ and μ are the usual elastic Lamé parameters and ν is the viscosity. In the domain of the Laplace transform variable s, (1) becomes

$$\tilde{\tau}_{kl} = \lambda(s)\tilde{e}_{ii}\delta_{kl} + \mu(s)\tilde{e}_{kl} \tag{2}$$

where the tilde denotes implicit dependence upon s and where

$$\lambda(s) = \frac{\lambda s + \mu K/\nu}{s + \mu/\nu}, \tag{3a}$$

$$\mu(s) = \frac{\mu s}{s + \mu/\nu}, \tag{3b}$$

$$K = \lambda + \frac{2}{3}\mu. \tag{3c}$$

The functions $\lambda(s)$, $\mu(s)$ are viscoelastic moduli and K is the usual elastic bulk modulus. In terms of $\lambda(s)$ and $\mu(s)$ the stress-strain relation (2) has exactly the same form as that for a Hookean elastic solid.

2.1 SCALAR EQUATIONS OF MOTION AND BOUNDARY CONDITIONS IN THE TRANSFORM DOMAIN

The correspondence principle assures us that if we solve an 'equivalent' elastic problem as a function of s using $\lambda(s)$ and $\mu(s)$ as moduli then we shall have constructed the Laplace transform of the solution to the viscoelastic problem. The equivalent elastic problem which we must solve is the problem of surface loading of a spherical self-gravitating earth model. The appropriate field equations for this problem are well known from the theory of elastic gravitational free oscillations (Backus 1967) and for momentum conservation and the gravitational field are respectively

$$0 = -\rho_0 \nabla \tilde{\phi}_1 - \tilde{\rho}_1 g_0 \mathbf{e}_r - \nabla(\tilde{\mathbf{u}} \cdot \rho_0 g_0 \mathbf{e}_r) + \nabla \cdot \tilde{\boldsymbol{\tau}} \tag{4a}$$

$$\nabla^2 \tilde{\phi}_1 = 4\pi G \tilde{\rho}_1 . \tag{4b}$$

In (4b) the density perturbation $\tilde{\rho}_1$ is obtained from the linearized continuity equation as

$$\tilde{\rho}_1 = -\rho_0 \nabla \cdot \tilde{\mathbf{u}} - \tilde{\mathbf{u}} \cdot (\partial_r \rho_0) \mathbf{e}_r \tag{4c}$$

where the momentum equation, in which the inertial force has been neglected, has also been linearized with respect to perturbations from a hydrostatic equilibrium background state (ρ_0, p_0, g_0) which satisfies

$$\nabla p_0 = -\rho_0 g_0 \mathbf{e}_r \tag{4d}$$

$$\nabla^2 \tilde{\phi}_0 = 4\pi G \rho_0 . \tag{4e}$$

In (4) ρ and g are density and gravitational acceleration, $\tilde{\mathbf{u}}$ is the displacement vector, $\boldsymbol{\tau}$ the stress tensor, ϕ the gravitational potential and $\mathbf{e}_r$ a unit vector in the radial direction. In (4a, b) the perturbation geopotential ϕ_1 will be the sum of two parts, ϕ_2 and ϕ_3, which are respectively the potential of the externally applied gravitational force field (the load) and that due to the internal redistribution of mass effected by the load induced deformation. It therefore follows that $\nabla^2 \phi_3 = 4\pi G \rho_1$ within the Earth whereas $\nabla^2 \phi_2 = 0$ in the same region. The first term on the right of (4a) is the total gravitational body force whereas the second term on the right is the buoyancy force, which would vanish identically if the Earth were neutrally stratified. The third term in (4a) can be written as $\nabla(u \partial_r \rho_0)$ and is the advection of prestress as a result of an initial elastic displacement (Love 1927). It may not be immediately obvious what role this term will play in the fluid limit and we have not made this role sufficiently clear in our past discussions of the viscoelastic problem. Its importance is clarified by defining a new stress $\tau^1 = \tau - \rho_0 g_0 u \mathbf{I}$ where $\mathbf{I}$ is the identity tensor and u is the radial displacement. The last two terms of (4a) then combine as $\nabla \cdot \tau^1$ and (4a) itself then looks like the momentum balance equation for a viscous fluid. The existence of the prestress term in (4a) is *required* in order that the correct boundary condition be satisfied in the viscous fluid limit.

We first seek solutions to equations (4) which describe the deformation of the radially stratified planet which is produced when a point mass load is placed on its surface. Since the tangential stress on the surface vanishes, the toroidal and poloidal motions decouple with the former being identically zero. Symmetry considerations then demand a solution with the

following vector harmonic decomposition

$$\mathbf{u} = \sum_{n=0}^{\infty} \left[U_n(r,s) P_n(\cos\theta)\mathbf{e}_r + V_n(r,s) \frac{\partial}{\partial\theta} P_n(\cos\theta)\mathbf{e}_\theta \right] \tag{5a}$$

$$\phi_1 = \sum_{n=0}^{\infty} \Phi_n(r,s) P_n(\cos\theta) \tag{5b}$$

$$\nabla\cdot\mathbf{u} = \sum_{n=0}^{\infty} \chi_n(r,s) P_n(\cos\theta)\ . \tag{5c}$$

Substitution of (5) into (4) then leads to the set of simultaneous ordinary differential equations discussed by Love (1911) and Alterman, Jarosch & Pekeris (1959) with the exception that our system lacks those terms derivative of the inertial force. With the understanding that U, V, Φ, χ, λ and μ respectively stand for $U_n(r,s)$, $V_n(r,s)$, $\Phi_n(r,s)$, $\chi_n(r,s)$, $\lambda(r,s)$, $\mu(r,s)$, equations (4) reduce to the following set of three coupled second-order equations

$$\ddot{\Phi} + \frac{2}{r}\dot{\Phi} - \frac{n(n+1)}{r^2}\Phi = -4\pi G(\rho_0\chi + \dot{\rho}_0 U) \tag{6a}$$

$$0 = -\rho_0\dot{\Phi} + \rho_0 g_0\chi - \rho_0\frac{d}{dr}(g_0 U) + \frac{d}{dr}(\lambda\chi + 2\mu\dot{U}) + \frac{\mu}{r^2}[4\dot{U}r - 4U + n(n+1)(-U - r\dot{V} + 3V)] \tag{6b}$$

$$0 = -\rho_0\Phi - \rho_0 g_0 U + \lambda\chi + r\frac{d}{dr}\left[\mu\left(\dot{V} - \frac{V}{r} + \frac{U}{r}\right)\right] + \frac{\mu}{r}[5U + 3r\dot{V} - V - 2n(n+1)V] \tag{6c}$$

in which the dots denote differentiation with respect to r, and

$$\chi = \dot{U} + \frac{2}{r}U - \frac{n(n+1)}{r}V \tag{6d}$$

$$\dot{g}_0 + \frac{2}{r}g_0 = 4\pi G\rho_0\,. \tag{6e}$$

Equations (6) are the complete set of equations in the transform domain which are to be solved in the mantle. In terms of the vector $\mathbf{Y} = (U_n, V_n, T_{rn}, T_{\theta n}, \Phi_n, Q_n)^t$ in which

$$\begin{aligned} T_{rn} &= \lambda\chi_n + 2\mu\dot{U}_n\,, \\ T_{\theta n} &= \mu\left(\dot{V}_n - \frac{1}{r}V_n + \frac{1}{r}U_n\right)\,, \\ Q_n &= \dot{\Phi}_n + \frac{(n+1)}{r}\Phi_n + 4\pi G\rho_0 U_n\,, \end{aligned} \tag{7}$$

are respectively the coefficients in the spherical harmonic expansions of radial and tangential stress and an auxiliary variable related to the radial gradient of the potential perturbation, equations (6) may be written in the standard form

$$\frac{dY}{dr} = \mathbf{A}\,\mathbf{Y} \tag{8}$$

in which the elements of the A matrix are

$$a_{1i} = \left(-\frac{2\lambda}{r\beta}, \frac{n(n+1)}{r}\frac{\lambda}{\beta}, \frac{1}{\beta}, 0, 0, 0\right) \tag{9a}$$

$$a_{2i} = \left(-\frac{1}{r}, \frac{1}{r}, 0, \frac{1}{\mu}, 0, 0\right) \tag{9b}$$

$$a_{3i} = \left(\frac{4}{r}\left[\frac{\gamma}{r} - \rho_0 g_0\right], \frac{-n(n+1)}{r}\left[\frac{2\gamma}{r} - \rho_0 g_0\right], -\frac{4\mu}{r\beta}\frac{n(n+1)}{r}, \frac{-\rho_0(n+1)}{r}, \rho_0\right) \tag{9c}$$

$$a_{4i} = \left(\frac{1}{r}\left[\rho_0 g_0 - \frac{2\gamma}{r}\right], -\frac{1}{r^2}\left[2\mu - n(n+1)(\gamma+\mu)\right], \frac{-\lambda}{r\beta}, \frac{-3}{r}, \frac{\rho_0}{r}, 0\right) \tag{9d}$$

$$a_{5i} = \left(-4\pi G\rho_0, 0, 0, 0, \frac{-(n+1)}{r}, 1\right) \tag{9e}$$

$$a_{6i} = \left(-4\pi G\rho_0 \frac{(n+1)}{r}, \frac{4\pi G\rho_0 n(n+1)}{r}, 0, 0, 0, \frac{n-1}{r}\right) \tag{9f}$$

with

$$\lambda = \lambda(r, s)$$

$$\mu = \mu(r, s)$$

$$\beta = \lambda(r, s) + 2\mu(r, s)$$

$$\gamma = \mu(r, s)\left[\frac{3\lambda(r, s) + 2\mu(r, s)}{\lambda(r, s) + \mu(r, s)}\right].$$

The solution 6-vector **Y** which solves (8) may be represented generally as a linear superposition of six linearly independent solutions. The combination coefficients are determined by the boundary conditions at the endpoints of the domain $0 \leqslant r \leqslant a$, where a is the planetary radius. Three of these boundary conditions are that U, V and Φ be regular at $r = 0$ and together they reduce the number of acceptable linearly independent solutions of (8) from six to three. To determine the remaining boundary conditions at $r = a$ we follow Longman (1963) and Farrell (1972) and treat the point mass load (γ) on the surface as a unit mass distributed uniformly across a disc of vanishingly small radius α. Expanding γ in a Legendre series gives

$$\gamma = \sum_{n=0}^{\infty} \Gamma_n P_n(\cos\theta) \tag{10a}$$

in which the Γ_n are given by (Hobson 1955; Longman 1963; Farrell 1972)

$$\Gamma_n = \frac{2n+1}{4\pi a^2} \tag{10b}$$

in the limit $\alpha \to 0$. If we assume that the surface point mass load is applied as a delta function in the time domain then in the Laplace transform domain the boundary conditions will be independent of the Laplace transform variable s. The required conditions are then (Longman 1963; Farrell 1972) that $\nabla\phi_2 \cdot \mathbf{e}_r$ change by $4\pi\gamma$ across $r = a$, that $(\nabla\phi_3 + 4\pi G\rho\mathbf{u}) \cdot \mathbf{e}_r$ be continuous at $r = a$, that the normal stress balance the applied load ($\tau_{rr}(a) = -\gamma g$) and that

the tangential stress vanish ($\tau_{r\theta}(a) = 0$). In terms of the appropriate Legendre coefficients, these conditions are

$$T_{rn}(a) = -g\Gamma_n \tag{11a}$$

$$T_{\theta n}(a) = 0 \tag{11b}$$

$$Q_n(a) = -4\pi G\Gamma_n \tag{11c}$$

which now suffice to determine U_n, V_n, and Φ_n throughout the Earth. In analogy with the surface loading problem for an elastic sphere, it is convenient to describe these coefficients in terms of a triplet of dimensionless scalar Love numbers (h_n, l_n, k_n) which are functions of r, n and s. The definition is

$$\begin{bmatrix} U_n(r,s) \\ V_n(r,s) \\ \Phi_{3,n}(r,s) \end{bmatrix} = \Phi_{2,n}(r) \begin{bmatrix} h_n(r,s)/g_0 \\ l_n(r,s)/g_0 \\ -k_n(r,s) \end{bmatrix}. \tag{12}$$

Using (12) the total potential perturbation may be written as

$$\Phi_{1,n} = -\Phi_{2,n} + \Phi_{3,n} = -\Phi_{2,n}(1 + k_n) \tag{13}$$

where $\Phi_{2,n}$ follows from the definition

$$\phi_2(\mathbf{r}) = \int \frac{G\gamma(\mathbf{r})d^2r'}{|\mathbf{r} - \mathbf{r}'|} \tag{14}$$

in which the integration is over the Earth's surface. Substituting for $\gamma(\mathbf{r})$ in terms of its Legendre expansion (10a) and using the addition theorem for spherical harmonics (e.g. Jackson 1962) one obtains

$$\phi_2(a,\theta) = \sum_{n=0}^{\infty} \frac{4\pi aG}{(2n+1)} \Gamma_n P_n(\cos\theta) \tag{15}$$

so that

$$\Phi_{2,n}(a) = \frac{4\pi aG\Gamma_n}{(2n+1)} = \frac{ag_0}{m_e} \tag{16}$$

in which g_0 is the gravitational acceleration at the Earth's surface and m_e is the Earth's mass.

The analysis given in (1–16) above is essentially identical to that in Peltier (1974) and we have repeated it here, and have in fact expanded it in places, in order to provide the basic material necessary for comprehension of the following sections. In these sections we will first discuss a sequence of simple earth models for which analytic solutions to the governing equations can be obtained. These solutions are rather useful since they reveal several important properties of the mechanism of viscous gravitational relaxation.

3 Love number spectra for earth models of increasing complexity

If the physical properties of the model earth are all constant then we may obtain solutions to (8) subject to (11) in terms of simple functions. Here we shall focus, first, upon three important versions of the homogeneous model which isolate fundamental features of the more general problem. Following discussion of these simple models we shall describe the Love number spectra obtained for more realistic earth models.

3.1 HOMOGENEOUS AND INCOMPRESSIBLE

We shall first consider the homogeneous incompressible model which has, for definiteness, the constant values of density, viscosity and elastic parameter listed in Table 1, which are those appropriate to the average earth. Since the model is incompressible $\nabla \cdot \mathbf{u} \equiv 0$ and since it has constant density $\partial_r \rho_0 = 0$ so that (4c) reduces to $\rho_1 = 0$ and (4a) and (4b) decouple. Equation (4b) reduces to

$$\nabla^2 \phi_1 = 0. \tag{17}$$

In an incompressible medium the dilatation $\Delta = \nabla \cdot \mathbf{u}$ goes to zero and λ goes to infinity in such a way that their product has a finite limit (Love 1911, section 154), i.e.

$$\lim_{\substack{\lambda \to \infty \\ \Delta \to 0}} (\lambda \Delta) = \Pi. \tag{18}$$

The incompressible form of the constitutive relation which replaces (2) is then

$$\tau_{kl} = \Pi \delta_{kl} + 2\mu e_{kl} \tag{19}$$

which, using the definition of e_{kl} and the fact that $\nabla \cdot \mathbf{u} = 0$ may be shown to have divergence,

$$\nabla \cdot \tau = \nabla \Pi - \mu \nabla \times \nabla \times \mathbf{u} \tag{20}$$

where $\mu = \mu(s)$ is as defined in (3b) and Π has the meaning of a mean normal stress. Using $\partial_r \rho_0 = 0$ and $\nabla \cdot \mathbf{u} = 0$, (4a) may be rewritten

$$0 = -\nabla(\rho_0 \phi_1 + \rho_0 g_0 \mathbf{u} \cdot \mathbf{e}_r - \Pi) - \mu \nabla \times \omega \tag{21}$$

where $\omega = \nabla \times \mathbf{u}$. The divergence of (21) is

$$0 = \frac{\rho_0}{\mu} \nabla^2 (\phi_1 + g_0 \mathbf{u} \cdot \mathbf{e}_r - \Pi/\rho_0). \tag{22}$$

For spheroidal motion with no ϕ dependence

$$\Pi = \sum_{n=0}^{\infty} \Pi_n(r, s) P_n(\cos\theta) \tag{23a}$$

$$\omega = \sum_{n=0}^{\infty} H_n(r, s)\, \partial_\theta P_n(\cos\theta) \mathbf{e}_\phi \tag{23b}$$

Table 1. Physical properties of the average earth.

Parameters	Symbol	Average value	Units
Density	ρ_0	5517	kg m^{-3}
Viscosity	ν	10^{22}	poise
S-wave velocity	V_S	5130	m s^{-1}
P-wave velocity	V_P	10 798	m s^{-1}
Lamé constants	μ	1.4519×10^{11}	N m^{-2}
	λ	3.5288×10^{11}	N m^{-2}
Gravitational acceleration at Earth's surface	g_0	9.82	m s^{-2}
Radius of the Earth	a	6.371×10^6	m

where

$$H_n = \dot{V}_n + \frac{1}{r} V_n - \frac{1}{r} U_n \,. \tag{23c}$$

Since the density is uniform, $g_0/r = \xi$, a constant where $\xi = 4\pi G\rho_0/3$. Using (5) and (23), equations (17) and (22) reduce to the following respective forms

$$\nabla_r^2 \Phi = 0 \tag{24}$$

$$\nabla_r^2 (\Phi + \xi r U - \Pi/\rho_0) = 0 \tag{25}$$

where $\nabla_r^2 = d^2/dr^2 + (2/r)d/dr - n(n+1)/r^2$. Also, the radial component of (21) is

$$\partial_r^2 (r^2 U) - n(n+1)U = (\rho_0/\mu) r^2 \partial_r (\Phi + \xi r U - \Pi/\rho_0) \tag{26}$$

in which the definition of the dilatation has been used to eliminate V. The solutions of (24) and (25) are respectively

$$\Phi = C_3 r^n \tag{27}$$

$$\Phi + \xi r U - \frac{\Pi}{\rho_0} = \frac{\mu}{\rho_0} C_1 r^n \,. \tag{28}$$

Substituting (28) into (26) we obtain an inhomogeneous o.d.e. for U which may be solved to give

$$U = \frac{C_1 n}{2(2n+3)} r^{n+1} + C_2 r^{n-1} \,. \tag{29}$$

Using (6d) and (7) we may obtain solutions for $V_n, T_{\theta n}, Q_n$, and $T_{rn} = \Pi_n + 2\mu(s)\dot{U}_n$. The solution 6-vector $\mathbf{Y}$ which solves the incompressible equivalent of (8) is then the following superposition of three linearly independent solutions.

$$\mathbf{Y} = \sum_{i=1}^{3} C_i \mathbf{y}_i \tag{30a}$$

where

$$\mathbf{y}_1 = \left(\frac{n r^{n+1}}{2(2n+3)}, \frac{(n+3) r^{n+1}}{2(2n+3)(n+1)}, \frac{\rho_0 \xi n r^{n+2} + 2\mu r^n (n^2 - n - 3)}{2(2n+3)}, \right.$$

$$\left. \frac{2\mu n (n+2) r^n}{2(2n+3)(n+1)}, 0, \frac{3\xi n r^{n+1}}{2(2n+3)} \right)^t \tag{30b}$$

$$\mathbf{y}_2 = \left(r^{n-1}, \frac{r^{n-1}}{n}, \rho_0 \xi r^n + 2\mu(n-1) r^{n-2}, \frac{2\mu(n-1)}{n} r^{n-2}, 0, 3\xi r^{n-1} \right)^t \tag{30c}$$

$$\mathbf{y}_3 = [0, 0, \rho_0 r^n, 0, r^n, (2n+1) r^{n-1}]^t \,. \tag{30d}$$

The constants $C_i \equiv C_i(n,s)$ in (30a) can be determined for fixed n and s by defining

$$\mathbf{c} = (C_1, C_2, C_3)^t \tag{31a}$$

$$\mathbf{b} = \left(\frac{-g(2n+1)}{4\pi a^2}, 0, \frac{-g}{m_e}(2n+1) \right)^t \tag{31b}$$

and

$$\mathbf{M} = \begin{pmatrix} \dfrac{\rho_0 \xi n a^{n+2} + 2\mu a^n (n^2 - n - 3)}{2(2n+3)} & \rho_0 \xi a^n + 2\mu(n-1)a^{n-2} & \rho_0 a^n \\ \dfrac{2\mu n(n+2)a^n}{2(2n+3)(n+1)} & \dfrac{2\mu(n-1)a^{n-2}}{n} & 0 \\ \dfrac{3\xi n a^{n+1}}{2(2n+3)} & 3\xi a^{n-1} & (2n+1)a^{n-1} \end{pmatrix}. \tag{31c}$$

The surface boundary conditions (11) then take the form

$$\mathbf{M}\mathbf{c} = \mathbf{b} \tag{31d}$$

and the constants C_i can be obtained from

$$\mathbf{c} = \mathbf{M}^{-1}\mathbf{b}. \tag{31e}$$

After considerable algebra we obtain the following explicit expressions for the coefficients C_i:

$$C_1(s) = \frac{2\rho_0 g_0 (n+1)(n-1)(2n+3)a^{-(n+1)}}{3m_e \beta(s)} \tag{32a}$$

$$C_2(s) = \frac{-\rho_0 g_0 n^2 (n+2) a^{-(n-1)}}{3m_e \beta(s)} \tag{32b}$$

$$C_3(s) = \frac{-g_0 \mu(s)(2n^2 + 4n + 3)}{m_e \beta(s)} a^{-(n+1)} \tag{32c}$$

in which $\beta(s) = a^{-1}[n\rho_0 g_0 + \mu(s)a^{-1}(2n^2 + 4n + 3)]$. Substituting these values for the C_i in (30), from their definitions (12) we obtain the surface load Love numbers for the incompressible model as

$$h_n(a,s) = \frac{-(2n+1)n\rho_0 g_0}{3\beta(s)a} \tag{33a}$$

$$k_n(a,s) = -1 + \frac{\mu(s)(2n^2 + 4n + 3)}{a^2 \beta(s)} \tag{33b}$$

$$l_n(a,s) = \frac{-\rho_0 g_0}{\beta(s)a}. \tag{33c}$$

In Fig. 1(a) we plot the spectrum $h_n(a,s)$ for various values of n. It will be seen by inspection that these spectra are characterized by asymptotes both for large and small values of s. As pointed out in Peltier (1974), the asymptote at large s, h_n^E, is the load Love number of the elastic sphere whereas the small s asymptote, h_n^∞, is such that the difference $(h_n^\infty - h_n^E)$ measures the total viscous relaxation which would occur if the point load were left on the surface for all time (Peltier 1976). For later purposes it is important to note that the procedure used here to construct the Love number spectra breaks down for s sufficiently small. This can be seen as follows: when $s \to 0$, $\mu(s) \approx \nu s$ from (3b) and this tends to zero with s, so that the second row of M in (31c) vanishes identically and the constants C_i cannot be determined from (31e) because $\mathbf{M}^{-1}$ does not exist. This difficulty occurs because for small s, or equivalently large time from the Tauberian theorems, the Maxwell solid effectively behaves like an inviscid fluid with vanishingly small tangential stress and indeterminate tangential displacement (see Section 3.3 below). The sixth-order system degenerates to a second order system and this must be solved explicitly in general to determine the $s = 0$ spectral asymptotes.

3.2 HOMOGENEOUS AND COMPRESSIBLE

A second analytic solution which can be found for a spherical homogeneous model is that in which the full effects of compressibility upon the deformation are included. This solution may be obtained by setting $\dot{\rho}_0 = 0$ and $\Delta = \nabla \cdot \mathbf{u}$ in (4a, b) to obtain

$$0 = -\rho_0 \nabla \phi_1 + \rho_0 g_0 \Delta \mathbf{e}_r - \nabla(\rho_0 g_0 \mathbf{u} \cdot \mathbf{e}_r) + (\lambda + 2\mu)\nabla\Delta - \mu \nabla \times \nabla \times \mathbf{u} \tag{34a}$$

$$\nabla^2 \phi_1 = -4\pi G \rho_0 \Delta. \tag{34b}$$

The curl and divergence of (34a) are respectively

$$\frac{\mu}{\rho_0} \nabla^2 \omega = g_0 \mathbf{e}_r \times \nabla \Delta \tag{35}$$

$$0 = 4\xi\Delta + \xi \mathbf{e}_r \cdot \nabla \times \omega + \frac{(\lambda + 2\mu)}{\rho_0} \nabla^2 \Delta \tag{36}$$

in which $\xi = g_0/r$ and $\omega = \nabla \times \mathbf{u}$. The scalar forms of (34b), (35) and (36) are respectively

$$\nabla_r^2 \Phi_n = -3\xi \chi_n \tag{37}$$

$$\nabla_r^2 H_n = \xi V_S^{-2} \chi_n \tag{38}$$

$$(\nabla_r^2 + \alpha_2)\chi_n = n(n+1)\xi V_P^{-2} H_n \tag{39}$$

in which $V_P^2 = V_P^2(s) = [\lambda(s) + 2\mu(s)]/\rho_0$, $V_S^2 = V_S^2(s) = \mu(s)/\rho_0$, $\alpha^2 = \alpha^2(s) = 4\xi V_P^{-2}(s)$, and we shall also define $\gamma^2 = \gamma^2(s) = 4n(n+1)\xi^2 V_P^{-2}(s) V_S^{-2}(s)$. Equations (38) and (39) may be combined to give

$$\nabla_r^2(\nabla_r^2 + \alpha^2)\chi = \frac{1}{4}\gamma^2 \chi. \tag{40}$$

Defining wavenumbers k and q by

$$2k^2(s) = \alpha^2(s) + \sqrt{\alpha^4(s) + \gamma^2(s)} \tag{41a}$$

$$2q^2(s) = \alpha^2(s) - \sqrt{\alpha^4(s) + \gamma^2(s)} \tag{41b}$$

then (40) has the equivalent form

$$(\nabla_r^2 + k^2)(\nabla_r^2 + q^2)\chi = 0. \tag{42}$$

This equation has regular solutions at $r = 0$ of the form $\chi = j_n(kr)$ and $\chi = j_n(qr)$ where j_n is the spherical Bessel function of the first kind and nth degree. The complete solution 6-vector $\mathbf{Y}$ can again be represented in the form (30a) in which the elements of $\mathbf{y}_1$ are determined using $\chi = j_n(kr)$ in (37), (38), (6d), (7) and (23c) to obtain this contribution to the elements of $\mathbf{Y} = (U_n, V_n, T_{rn}, T_{\theta n}, \Phi_n, Q_n)^t$. This particular solution is

$$\begin{aligned}
U_n &= -(k^2 r)^{-1}\,[n(n+1)Cj_n(kr) + krj_n'(kr)] \\
V_n &= -(k^2 r)^{-1}\,[(1+C)j_n(kr) + Ckrj_n'(kr)] \\
T_{rn} &= \lambda j_n(kr) + 2\mu\,[n(n+1)C(kr)^{-1}\,\{(kr)^{-1}j_n(kr) - j_n'(kr)\} - j_n''(kr)] \\
T_{\theta n} &= -\mu C j_n(kr) + 2\mu\,[(1+C)(kr)^{-1}\,\{(kr)^{-1}j_n(kr) - j_n'(kr)\} - Cj_n''(kr)] \\
\Phi_n &= 3\xi k^{-2} j_n(kr) \\
Q_n &= 3\xi(1 - nC)(1+n)(k^2 r)^{-1} j_n(kr)
\end{aligned} \tag{43}$$

in which $C = -\xi V_S^{-2} k^{-2}$ and j_n' and j_n'' are the first and second derivatives of the spherical Bessel function respectively. The second linearly independent solution $\mathbf{y}_2$ has exactly the same form as (43) but with k replaced by q everywhere. The third of the required three linearly independent solution 6-vectors of which the complete solution $\mathbf{Y}$ is composed is

$$\mathbf{y}_3 = \begin{pmatrix} nr^{n-1} \\ r^{n-1} \\ 2\mu n(n-1)r^{n-2} \\ 2\mu(n-1)r^{n-2} \\ -n\xi r^n \\ -2n(n-1)\xi r^{n-1} \end{pmatrix}. \tag{44}$$

The three linearly independent solutions obtained above will be recognized as those described by Gilbert & Backus (1968) for the corresponding free oscillations problem, the sole differences being that factors dependent upon the existence of the inertial force in their work do not appear in ours and our moduli $\mu(s)$ and $\lambda(s)$ are frequency dependent.

Given the new $\mathbf{y}_i$ required in the general solution of the compressible problem we may proceed to determine the values of the combination coefficients C_i which are required in the linear superposition (30a) to satisfy the boundary conditions. This proceeds as in the last example and leads to analytic (though extremely complicated) expressions for the Love numbers $h_n(s), l_n(s), k_n(s)$. In Fig. 1(1b) we compare the Love number spectrum with $n = 60$, of the homogeneous compressible model to that for the homogeneous incompressible model. Inspection shows that in the large s elastic limit the compressible model exhibits considerably enhanced deformation, whereas in the small s infinite time limit the asymptotic deformation of the two models is identical. The reason for the equality of the isostatic response in these two models will be explored in the next subsection. In agreement with the point noted previously in connection with our discussion of the incompressible model we note that our procedure for calculating Love numbers again fails in the $s = 0$ limit since $k \to q$ and $\mathbf{y}_1$ and $\mathbf{y}_2$ are no longer linearly independent.

3.3 INHOMOGENEOUS BUT INVISCID

Our ability to provide a direct treatment of inviscid models is important for three reasons: first, since the real Earth possesses an essentially inviscid outer core, we are obliged to calculate the deformation in such regions directly. Secondly, and as pointed out in each of the preceding sections, our method for calculating Love numbers in the $s = 0$ limit breaks down. In this limit the deformation has reached isostatic equilibrium and since this state of no motion must be independent of viscosity we can compute it under the assumption $\nu = 0$ as we shall see. The last reason for the importance of this calculation is that an accurate calculation of the isostatic response is crucial if the viscoelastic model is to be used to predict gravity anomalies and stress.

Inspection of (3b) shows that the limits $s \to 0$ and $\nu \to 0$ are equivalent in the sense that in either limit the shear modulus $\mu(s)$ vanishes. Under this assumption the field equations (4a–c) reduce to the following forms:

$$0 = -\rho_0 \nabla \phi_1 - \rho_1 g_0 \mathbf{e}_r - \nabla p \tag{45a}$$

$$\nabla^2 \phi_1 = 4\pi G \rho_1 \tag{45b}$$

$$\rho_1 = -\rho_0 \nabla \cdot \mathbf{u} - \mathbf{u} \cdot (\partial_r \rho_0) \mathbf{e}_r \tag{45c}$$

where we have introduced a pressure field (mean normal stress) through the association $p = \mathbf{u} \cdot \rho_0 g_0 \mathbf{e}_r - K e_{ii}$ in (4a) with $\mu = 0$. The static deformation of an inviscid fluid part of the Earth has most recently been discussed by Dahlen & Fels (1978) whose analysis agrees with previous conclusions of Smylie & Mansinha (1971), Chinnery (1975) and Crossley & Gubbins (1975). There it is shown that fluid particles undergoing a quasi-static deformation experience changes neither of pressure nor of density as the deformation proceeds. It therefore follows that the dilatation is zero everywhere. Substituting $\nabla \cdot \mathbf{u} = 0$ in (45c), and expanding all variables in spherical harmonics, equations (45a, b) then reduce to

$$d_r^2 \Phi + \frac{2}{r} d_r \Phi - \left[\frac{n(n+1)}{r^2} + \frac{4\pi G \rho_0}{g_0} \right] \Phi = 0 \tag{46a}$$

$$U = -\Phi / g_0 . \tag{46b}$$

In (46b) U is now to be interpreted as the displacement of an equipotential, isobaric, or material surface. Using (7) we may reduce (46a) to a set of two simultaneous ordinary differential equations in the components of the 2-vector $\mathbf{Y} = (\Phi_n, Q_n)^t$ as

$$\frac{dY}{dr} = \mathsf{A}\mathbf{Y} \tag{47a}$$

with

$$\mathsf{A} = \begin{pmatrix} 4\pi G \rho_0 / g_0 - (n+1)/r & 1 \\ \dfrac{8\pi G \rho_0 (n-1)}{g_0 r} & \dfrac{(n-1)}{r} - \dfrac{4\pi G \rho_0}{g_0} \end{pmatrix} . \tag{47b}$$

The solution of the relaxation problem for realistic earth models requires matching of solutions (47a) for the outer core with solutions of (8) for the mantle across the core–

mantle boundary (CMB). The matching conditions are the same as those described by Smylie & Mansinha (1971) and later authors. If $\Phi_n^c(b^-)$ and $Q_n^c(b^-)$ are solutions of (47a) just below the CMB then the solution just above the CMB may be expressed as

$$\begin{bmatrix} U_n(b^+) \\ V_n(b^+) \\ T_{rn}(b^+) \\ T_{\theta n}(b^+) \\ \Phi_n(b^+) \\ Q_n(b^+) \end{bmatrix} = C_1 \begin{bmatrix} -\Phi_n^c(b^-)/g(b) \\ 0 \\ 0 \\ 0 \\ \Phi_n^c(b^-) \\ Q_n^c(b^-) \end{bmatrix} + C_2 \begin{bmatrix} 0 \\ 1 \\ 0 \\ 0 \\ 0 \\ 0 \end{bmatrix} + C_3 \begin{bmatrix} 1 \\ 0 \\ \rho_0(b^-)g_0(b) \\ 0 \\ 0 \\ 4\pi G\rho_0(b^-) \end{bmatrix} \tag{48}$$

where b is the radius of the core–mantle boundary and the C_i are to be determined by the boundary conditions at the Earth's surface. The last two constants determine a discontinuity of isobaric surface displacement across the CMB as discussed in the above cited references.

In an inviscid fluid part of the Earth in which the density is constant, $\dot{\rho}_0 = 0$, and (47) admits solutions of the form

$$\mathbf{Y} = \begin{pmatrix} \Phi_n \\ Q_n \end{pmatrix} = \begin{pmatrix} r^n \\ 2(n-1)r^{n-1} \end{pmatrix} . \tag{49}$$

The solution (49) may in fact be employed as a starting solution for sufficiently small r in the inviscid fluid. This starting solution is then propagated to the CMB using (47), the boundary condition (48) is applied, and the mantle 6-vector is then propagated to the Earth's surface using (8). The surface boundary conditions (11) are then applied to determine the C_i.

The above analysis can be employed directly to calculate the surface load Love numbers h_n^∞ and k_n^∞ which determine the isostatic response, a fact which has not been demonstrated previously. With $s = 0$ (or equivalently $\nu = 0$) the homogeneous earth models discussed in the last two subsections degenerate to the same incompressible inviscid fluid. The isostatic solutions can therefore be obtained by solving (45a) and (45b) with $\rho_1 = 0$ and subject to the normal surface boundary conditions. This is equivalent to setting $b = a$ in (48) and requiring that the result satisfy (11) in order to determine the C_i. Some algebra yields

$$\begin{aligned} C_1 &= 0 = \Phi_n \\ C_2 &= \text{indeterminate} = V_n \\ C_3 &= U_n = \frac{-(2n+1)}{4\pi a^2 \rho_0(a)} . \end{aligned} \tag{50}$$

From (12) the 'isostatic' Love numbers for the homogeneous models (whether compressible or incompressible) are then

$$h_n^\infty = \frac{-(2n+1)}{3} \tag{51a}$$

$$k_n^\infty = -1 . \tag{51b}$$

These formulae are in accord with the results shown in Figs 1(1a) and 1(1b) for the spectral asymptotes in small values of s. In fact, these are the same results when $\mu(s)$ is taken to be

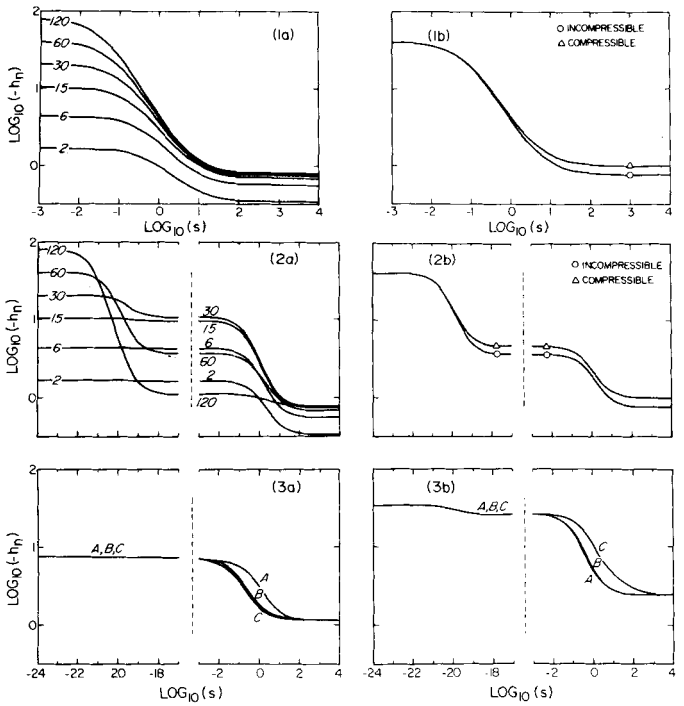

Figure 1. (1a) shows the Love number spectrum $h_n(a,s)$ for the homogeneous incompressible earth model. The angular order n of the Legendre harmonic is marked on each curve. (1b) illustrates the effect of compressibility on the spectrum for angular order $n = 60$. In (2a) we show the effect on these spectra of the presence of the lithosphere. Note that the large s (elastic) and small s (isostatic) asymptotes are the same as those shown in (1a). (2b) shows the effect of compressibility on these spectra for angular order $n = 60$. In (3a) we show $h_n(a,s)$ spectra for $n = 6$ for viscosity models L1(A), L2(B) and L3(C) described in the text. (3b) compares spectra for $n = 30$ of the same models.

zero in equations (33a,b). For realistic inhomogeneous earth models, deformations of large angular order n effectively see only the topmost layer of the model so that

$$\lim_{n\to\infty} h_n^\infty = -\frac{(2n+1)}{3}\frac{\bar{\rho}}{\rho_0(a)} \tag{52a}$$

$$k_n^\infty = -1 \tag{52b}$$

where $\bar{\rho}$ is the average density of the planet. In the next subsection we shall investigate the important effect upon the isostatic response which is introduced by the presence of the surface lithosphere.

3.4 EFFECT OF THE LITHOSPHERE UPON THE ISOSTATIC RESPONSE

On the basis of the discussion in the preceding subsection (equations 51a, 52a) it is clear that all earth models in which the viscosity is everywhere finite are characterized by the property that the surface load Love number h_n^∞ diverges to negative infinity as the Legendre degree, n, increases. From (51a) the divergence is essentially linear in n. Inspection of (5a) and (12) reveals that a consequence of this divergence is that the infinite series expansion for the

radial displacement will fail to converge for small θ, diverging in fact to negative infinity at $\theta = 0$. Recognizing that such large displacements may violate the linearity assumption upon which the field theory is based, the divergence of the infinite time response of the planet to an applied surface point mass load is nevertheless exactly what one should expect physically. Since the point mass occupies no volume it has infinite density and must therefore sink to the centre of the inviscid planet, this being the only location where it will feel no net force. Any surface load of finite surface area would, however, induce only a finite subsidence beneath it, the finite spatial scale of the load serving to clip the contribution to the response of the Love numbers h_n^∞ with large n.

Even for the point mass load, though, there exists a property of realistic earth models which removes the singularity from the infinite time response at small θ. This property concerns the tendency for the viscosity of the planet to obtain very high values in a thin layer near the surface called the lithosphere. Physically the region exists as a combined consequence of the exponential dependence of viscosity upon temperature and the thermal boundary layer nature of the mantle convective circulation which localizes a sharp increase of temperature (of $\approx 1500°C$) to the upper 100 km of the planet (e.g. Peltier 1980). Below this lithosphere, in which the radial temperature gradient is small (adiabatic), the viscosity of the upper mantle is relatively uniform and equal to about 10^{22} poise (e.g. Peltier 1974; Peltier & Andrews 1976; Peltier *et al.* 1978). As one approaches the upper surface of the planet from below the sharp drop in temperature combined with the thermally activated nature of the creep phenomenon effects a nominal viscosity increase which may be somewhat in excess of 10 orders of magnitude (making no allowance for effects of hydration, etc.).

A viscoelastic lithosphere may be included in the previous homogeneous models by employing a two 'layer' approximation in which the viscosity of the lithosphere ν_L is large compared to the viscosity of the mantle ν_M so that for $\mu/\nu_L \ll s \ll \mu/\nu_M$ the lithosphere behaves as an elastic solid with $\lambda_L(s) \simeq \lambda$ and $\mu_L(s) \simeq \mu$. In order to illustrate the effect of such a region on the Love number spectra we shall consider, for definiteness, an earth model in which the top 120 km have a viscosity which is 20 orders of magnitude higher than that of the mantle (i.e. $\nu_L = 10^{42}$ P). If we assume the model to be incompressible then the governing equations for both lithosphere and mantle are the same as those employed in Section (3.1). At the mantle–lithosphere interface all field variables must be continuous. As in our discussion of the homogeneous model, the field equations are valid only for $s \gtrsim \mu/\nu_M$ since for smaller s the mantle begins to behave inviscidly. In this range of s we treat the mantle explicitly as an inviscid fluid in which the solutions have the same form as discussed in the last subsection. Then the boundary conditions between mantle and lithosphere for $s \lesssim \mu/\nu_M$ are the same as those between the fluid core and the mantle.

Love number spectra $h_n(a,s)$ for this model are shown in Fig. 1.2(a), inspection of which shows that the individual spectra are characterized by two distinct relaxations, one for large s and one for small. These two relaxations are associated with the mantle and lithosphere respectively. Comparison of the large s asymptotes h_n^E and the small s asymptotes h_n^∞ of these spectra with those shown in Fig. 1(1a) for the model without lithosphere, shows that they are identical. The new spectra for the two-layer model differ from those in Fig. 1(1a) by the existence of the extensive intermediate asymptote in the range $10^{-17} \leqslant s \leqslant 10^{-3}$. This new asymptote, which we may denote by h_n^L, would become equal to h_n^∞ for a model in which the lithospheric viscosity was infinite. In practice, for most applications, ν_L is so large that it may be treated as effectively infinite, thus the h_n^L *are* the effective h_n^∞. Fig. 1.2(a) shows that the extent of the influence of the presence of the lithosphere is a strong function of n. For small n the deformation wavelength is so long that the lithospheric influence is

negligible; the entire relaxation takes place in the mantle. For $n \gtrsim 30$ the effect of the lithosphere on the spectrum becomes more pronounced and is such as to produce a marked decrease of h_n^L. For $n \geqslant 150, h_n^L \simeq h_n^E$ (convergence with n) and the load is entirely supported by the lithosphere. Such short wavelengths are oblivious of the mantle and the relaxation takes place only at long times (small s) within the lithosphere itself.

The effect of compressibility on these spectra is illustrated for a single example ($n = 60$) in Fig. 1(2b). As previously the compressible model has the largest elastic response (large s) but both models have the same isostatic (small s) asymptote. The intermediate states h_n^L for the two-layer model are also affected by compressibility and the sense is again such as to enhance the response. Given a large contrast between the viscosities of mantle and lithosphere the magnitudes of the h_n^L are determined entirely by lithospheric thickness. In summary then, the effect of a surface lithosphere in which the viscosity is effectively infinite is to suppress the viscous gravitational relaxation of all surface deformations of sufficiently short wavelength. It is therefore an important effect to keep in mind when the isostatic response of a planetary model is considered.

3.5 LOVE NUMBER SPECTRA FOR A REALISTIC EARTH MODEL

In the past subsections we have described Love number spectra for earth models which were sufficiently simple that analytical solutions to the boundary value problem were possible. For realistic earth models the system of equations (8) must be solved numerically and to do this we have employed the shooting method described by Peltier (1974). If we are interested in earth models which are effectively incompressible we may obtain a modified version of (8) merely by setting $\lambda\chi = \Pi$ and $\chi = 0$ in (6). The simultaneous equations for the incompressible model then have exactly the form (8) except that in the matrix A the parameters λ/β, $1/\beta$ and γ are replaced respectively by 1, 0 and $3\mu(r,s)$. An earth model is completely described by the set of functions $\rho_0(r), g_0(r), \nu(r)$, $\mu(r)$ and $\lambda(r)$ (if the model is compressible). These functions are assumed known at a discrete set of N sampling points r_i, $1 \leqslant i \leqslant N$ and are determined at intermediate radii by linear interpolation although cubic splines would probably be preferable. It is rather important in the viscous gravitational relaxation problem that a model consisting of a stack of homogeneous layers not be adopted since each discontinuity introduces a new relaxation time into the relaxation spectra to be discussed in the next section.

Fig. 1(3a,b) shows Love number spectra for three compressible and realistic earth models each of which has $\rho(r)$, $\lambda(r)$, $\mu(r)$ profiles which are the same as model 1066B of Gilbert & Dziewonski (1975). The viscosity profiles for the three viscosity models are shown in Fig. 7. Each has a 120 km thick lithosphere and a 10^{22} poise upper mantle. The differences between models are in the lower mantle beneath the seismic discontinuity at 670 km depth and in the presence or absence of a low viscosity channel beneath the lithosphere. Model 1 has $\nu = 10^{22}$ P through the mantle, model 2 has a lower mantle with $\nu = 10^{23}$ P, while model 3 is the same as 2 but includes a low viscosity zone which is 10^2 km thick in which $\nu = 10^{20}$ P. Inspection of Fig. 1(3) shows that all models have the same h_n^E and h_n^L asymptotes for the reasons discussed previously. In Fig. 1(3a) the spectra are for $n = 6$ and it will be observed that the relaxation for model 1 is centred about a larger value of s than for either models 2 or 3. This is simply because the $n = 6$ harmonic samples the lower mantle and since model 1 has the lowest viscosity there it relaxes with the shortest characteristic time. The effect of the low viscosity zone is seen to be negligible for $n = 6$. In Fig. 1(3b) the spectra are for $n = 30$ and in this case model 3 shows a faster relaxation than either models 1 or 2. The $n = 30$ harmonic does not 'see' the lower mantle so that the only important differences between

models are those in the upper mantle. The low viscosity zone in model 3 therefore forces the $n = 30$ relaxation for this model to proceed most quickly whereas the spectra for models 1 and 2 are almost indistinguishable.

An extremely important result which follows from the calculations in this subsection is the determination of the asymptotic values of the surface load Love numbers which obtain in the limit $s \to 0$. We have previously denoted these numbers by h_n^L, l_n^L, and k_n^L for models with lithospheres and noted that it is in terms of these asymptotic values that the isostatic response to a given surface load is described. As we shall see later in Section 5.2, h_n^L and k_n^L are both required in the calculation of free air gravity anomalies. Another important application of these numbers which we shall discuss briefly here is in the determination of the polar motion forced by the glaciation–deglaciation cycle of the current ice age. This problem has recently been discussed in Sabadini & Peltier (1981) where it is shown that the Laplace transformed excitation function for a viscoelastic earth is proportional to $1 + k_2(s)$. Therefore if $k_2 \to -1$ in the limit of infinite time (or equivalently $s \to 0$) as obtains for a homogeneous viscoelastic earth (equation 51b), then the net motion of the pole over a single glaciation – deglaciation cycle will vanish. However, to the extent that $1 + k_2$ differs from zero in the infinite time limit the rotation pole will execute a continuous slow drift relative to the geography as the surface ice load appears and disappears. In Sabadini & Peltier (1981) $k_2(s)$ was approximated as

$$k_2(s) = -\frac{(1 - l_s)}{1 + \bar{\mu}(s)}$$

for realistic earth models with $\bar{\mu}(s)$ taken as the normalized shear modulus for a homogeneous Maxwell model. This approximation was taken from Munk & MacDonald (1960) who express the 'isostatic factor' l_s as $l_s = 4(b/a)(1 - \rho^1/\rho_0)$, in which b is the crustal thickness, a the Earth's radius, ρ^1 the crustal density, and ρ_0 the average density of the planet. Using this formula, Sabadini & Peltier (1981) estimated $l_s \simeq 0.006$ and obtained an average speed of polar wander of $0.2°/10^6$yr away from the centre of glaciation (see fig. 6 of Sabadini & Peltier). Using the general formalism developed here we have calculated isostatic factors for realistic earth models from $l_s = 1 + k_2^L$. For a realistic earth model we obtain $l_s \simeq 0.009$ (Table 2) which implies an average speed of polar wander during the ice age which may be somewhat larger than $0.3°/10^6$yr. Although this new result does not greatly alter the conclusion of Sabadini & Peltier (1981), it is nevertheless important. True polar wander induced by this process could well be that which is observed in the recent palaeomagnetic record. If the rotation pole should wander sufficiently in response to this forcing, it could conceivably induce a large-scale melting in Antarctica and a marked change in global climate.

Table 2. Infinite time Love numbers for model 1066B with a 120 km thick lithosphere that has infinite viscosity.

n	$-h_n^L$	$-nk_n^L$
0	0.140	0
1	0.716	0
2	2.847	1.982
6	7.412	5.945
15	17.305	14.470
30	25.508	21.315
60	12.639	9.832
∞	5.078	2.706

4 Relaxation spectra for earth models of increasing complexity

Having found solutions to the equivalent elastic problem in the domain of the Laplace transform variable s, in the form of Love number spectra, the first step in the application of the correspondence principle to the surface loading problem has been completed. The final step is to invert these spectra into the time domain. Although several approximate methods are available in terms of which the time domain forms of these spectra may be evaluated, it turns out that the inversion may be carried out exactly using a normal mode formalism first described in Peltier (1976). We will first provide a brief review of this formalism here and then go on to apply it to the same sequence of simple earth models discussed in the last section.

4.1 THE NORMAL MODE FORMALISM FOR VISCOUS GRAVITATIONAL RELAXATION

Consider the homogeneous boundary value problem associated with the simultaneous set of o.d.e.'s (8). For the homogeneous problem the surface boundary conditions which replace (11) are

$$T_{rn}(a) = T_{\theta n}(a) = \Phi_n(a) = 0 \tag{53}$$

and will obtain only for the values of s which satisfy the secular condition

$$\det(T^j_{rn}, T^j_{\theta n}, \Phi^j_n) = 0 \tag{54}$$

where T^j_{rn}, $T^j_{\theta n}$ and Φ^j_n $(j = 1,3)$ denote the three linearly independent surface values of the functions in (53) which are obtained by propagating each of the three linearly independent starting solutions of (8) to the Earth's surface from the starting depth. The set of s values which solve (54) constitute a discrete set of eigenvalues $\{s^n_i\}$ each of which is the inverse relaxation time of a particular normal mode of viscous gravitational relaxation. In terms of these eigenvalues of the homogeneous problem, the s-domain form of the solution to the inhomogeneous boundary value problem has the following Laurent series form

$$h_n(s) = h^{\mathrm{E}}_n + \sum_{i=1}^{m} \frac{r^n_i}{s + s^n_i} \tag{55}$$

where m is the number of eigenvalues found for fixed Legendre degree n. The eigenvalues s^n_i are therefore poles of the integrand in the contour integral which defines $h_n(t)$. As we shall show below, each of the poles $s = -s^n_i$ lies on the negative real axis in the complex s-plane so that inversion of $h_n(s)$ gives

$$h_n(t) = h^{\mathrm{E}}_n \delta(t) + \sum_{i=1}^{m} r^n_i \exp(-s^n_i t). \tag{56}$$

The constants r^n_i are just the residues at the poles $s = -s^n_i$ in the solution to the inhomogeneous problem. They may be determined by solving the inhomogeneous problem to determine

$$h_n(s^n_j) - h^{\mathrm{E}}_n = \sum_{i=1}^{m} \frac{r^n_i}{s^n_j + s^n_i} \tag{57}$$

in which the only unknowns are the r_i^n. Defining

$$m_{ij} = \frac{1}{s_j^n + s_i^n} \tag{58a}$$

$$h_n^V(s) = h_n(s) - h_n^E, \tag{58b}$$

equations (57) may be rewritten as

$$h_n^V(s_j^n) = m_{ij} r_i^n \tag{58c}$$

so that

$$r_i^n = m_{ij}^{-1} h_n^V(s_j^n). \tag{58d}$$

All terms in (56) are now known and we have an exact time domain form of the Love number spectra which are required to describe the response of an earth model to gravitational interaction with a point mass load which is brought to its surface at $t = 0$ and instantaneously removed. In the following subsections we shall describe the eigenspectra s_i^n in terms of plotted points in the s–n plane, to which we shall refer as relaxation diagrams.

4.2 RELAXATION SPECTRUM FOR AN INCOMPRESSIBLE HOMOGENEOUS MODEL

For homogeneous boundary conditions, the determinant of the matrix M in (31d) must vanish. Since this has the explicit form (from 31c)

$$\det \mathsf{M} = \frac{2\mu(s)(n-1)(2n+1)a^{3n-1}}{n(n+1)(2n+3)} \{\rho_0 \xi n + \mu(s)(2n^2+4n+3)a^{-2}\} \tag{59}$$

the eigenvalues of the homogeneous problem are solutions of

$$\mu(s) = \frac{-\rho_0 n \xi a^2}{(2n^2+4n+3)} \tag{60}$$

or are those values of s which make $\mu(s) \equiv 0$. Since $\mu(s) = \mu s/(s + \mu/\nu)$ from (3b), the non-zero eigenvalues are

$$s^n = \frac{-1}{\nu\left(\dfrac{2n^2+4n+3}{n\rho_0 g_0 a} + \dfrac{1}{\mu}\right)} \tag{61}$$

in which μ is the elastic Lamé parameter.

The eigenvalue for a purely viscous incompressible model may be found by employing the appropriate compliance $\mu(s) = \mu s$ in (60) to obtain

$$s^{Vn} = \frac{-n g_0 \rho_0 a}{\nu(2n^2+4n+3)} \tag{62}$$

which is the same as the expression for the inverse decay time of a viscous sphere deduced directly from the hydrodynamic equations by Peltier (1974). Using the non-dimensionalization scheme in Table 3 and employing the average values of ρ_0, g_0, μ and ν for the real Earth (Table 1), dimensionless values of s^n and s^{Vn} have been calculated for several values of the

Table 3. Non-dimensionalization scheme.

Length	$a = 6.371 \times 10^6$ m
Time	1000 yr (3.153×10^{10} s)
Density	$\bar{\rho} = 5517$ kg m^{-3}
Stress	$\mu^* = \pi G \bar{\rho}^2 a^2$
Gravitational acceleration	$\mu^*/(a\bar{\rho})$
Gravitational potential	$(\mu^*/\bar{\rho})$
Elastic parameter	μ^*

Table 4. Comparison of the viscoelastic eigenvalues s^n and the viscous eigenvalues s^{Vn} for a homogeneous earth model.

n	$\bar{s}^n$	$\bar{s}^{Vn}$	Percentage difference
2	−0.9165	−1.1458	25
4	−0.7196	−0.8537	18
6	−0.5766	−0.6597	14
8	−0.4784	−0.5342	10
10	−0.4080	−0.4479	10
50	−0.1023	−0.1046	2
100	−0.0527	−0.0534	1
500	−0.0108	−0.0108	< 0.1

angular order and are compared in Table 4. Inspection of this table shows that by neglecting the elastic coupling term in the denominator of (61) all relaxation times are shortened. The error committed in making the viscous approximation is approximately 25 per cent for $n = 2$ and 10 per cent for $n = 10$.

A plot of the relaxation spectrum for the homogeneous incompressible model is shown in Fig. 2(a) in which the values of s^n are normalized according to Table 2 so that $1/s^n$ gives the relaxation time in kyr. For sufficiently high angular order $n(n \gtrsim 25)$, the deformation 'sees' the Earth as a flat half-space and the relaxation time may be approximated as

$$\tau^n = \frac{-1}{s^n} \simeq \frac{2\nu n}{\rho_0 g_0 a} . \tag{63}$$

This is the same as the result obtained by Haskell (1935), McConnell (1965), and other authors. When n is small the effect of sphericity is to cause the relaxation spectrum to deviate from the linear relation (63) in such a way that relaxation time is increased.

The eigenfunctions corresponding to the eigenvalues s^n which satisfy the secular condition may be found to within an arbitrary multiplicative constant by choosing $C_1(s^n) = A$ for example and then using any two of the three linearly independent row vectors of M to find $C_2(s^n)$ and $C_3(s^n)$ in terms of A (say). Substitution of these results into (30) with $\mu = \mu(s^n)$ then yields

$$U_n(r, s^n) \propto nr^{n+1} - \frac{a^2 n^2 (n+2) r^{n-1}}{(n+1)(n-1)} \tag{64a}$$

$$V_n(r, s^n) \propto \frac{(n+3)}{(n+1)} r^{n+1} - \frac{a^2 n(n+2)}{(n+1)(n-1)} r^{n-1} \tag{64b}$$

$$\Phi_n(r, s^n) \propto \frac{3\xi n a^2}{(n+1)(n-1)} r^n \tag{64c}$$

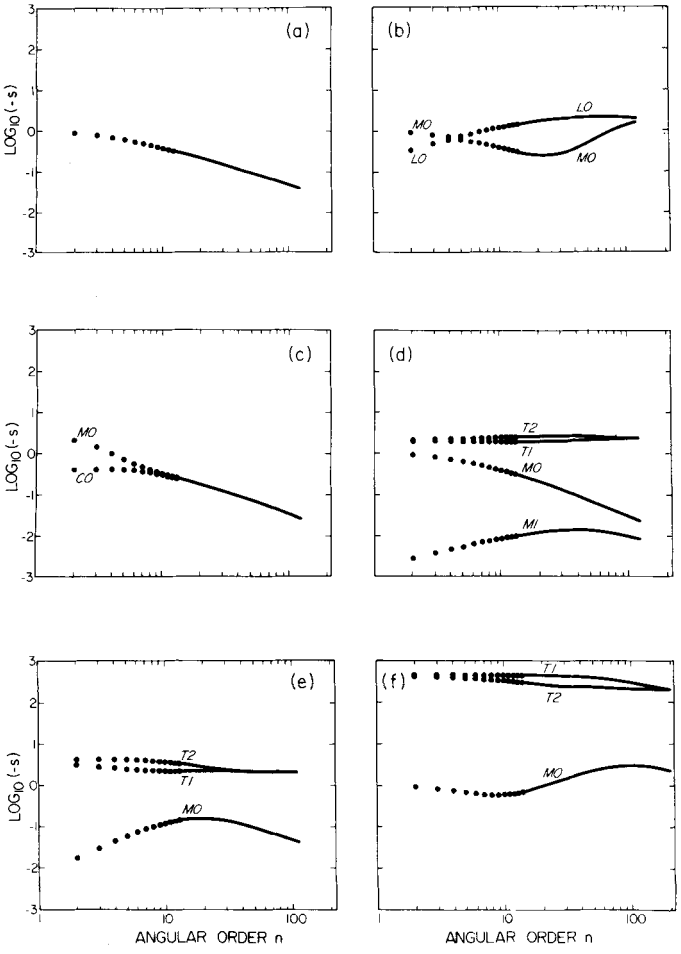

Figure 2. Relaxation diagrams (a–f) for the six incompressible earth models whose viscoelastic structures are shown in Fig. 4. (a) is the spectrum for the homogeneous model, (b) includes the effect of a lithosphere, (c) the effect of a fluid core, (d) a simple density discontinuity, (e) a high viscosity interior region, and (f) a low viscosity region adjacent to the surface. On all plates the relaxation time $\tau = s^{-1}$ is measured in units of 10^3 yr.

and similarly for $T_m(r, s^n)$, $T_{r\theta}(r, s^n)$ and $Q_n(r, s^n)$. From these eigenfunctions we may construct the differential kernels which are crucial to the formulation of the inverse problem for mantle viscosity and which are rather useful for purposes of mode identification (Peltier 1976). We shall show some examples of these kernels here.

In the s-domain the shear energy distribution is just

$$\zeta = 2\mu(s)\Delta_{ij}\Delta_{ij}^{*} \tag{65}$$

in which

$$\Delta_{ij} = \frac{1}{2}(\partial_i u_j + \partial_j u_i) - \frac{1}{3}\partial_k u_k \delta_{ij} \tag{66}$$

is the strain deviator and * denotes complex conjugation. The radial part of $\Delta_{ij}\Delta_{ij}^{*}$ is just

$$K_n = \frac{1}{3}(2\partial_r U_n - F_n)^2 + r^{-2}n(n+1)(r\partial_r V_n - V_n + U_n)^2 + r^{-2}n(n-1)(n+1)(n+2)V_n^2 \quad (67)$$

where

$$F_n = r^{-1}[2U_n - n(n+1)V_n]$$

and the normalized shear kernel is just

$$K(r) = \left[\frac{K_n[(\mu^2/\nu)/(s+\mu/\nu)^2]}{\int_0^a K_n[(\mu^2/\nu)/(s+\mu/\nu)^2]\, r^2 dr}\right]_{s=s^n} . \quad (68)$$

As described in Peltier (1976) the importance of $K(r)$ is that one may use it to calculate the shift in a free decay pole which is forced by a perturbation of the viscosity profile $\delta\nu(r)$ by computing

$$\frac{\delta s}{s} = -\int_0^a K(r) r^2 \frac{\delta\nu(r)}{\nu(r)}\, dr . \quad (69)$$

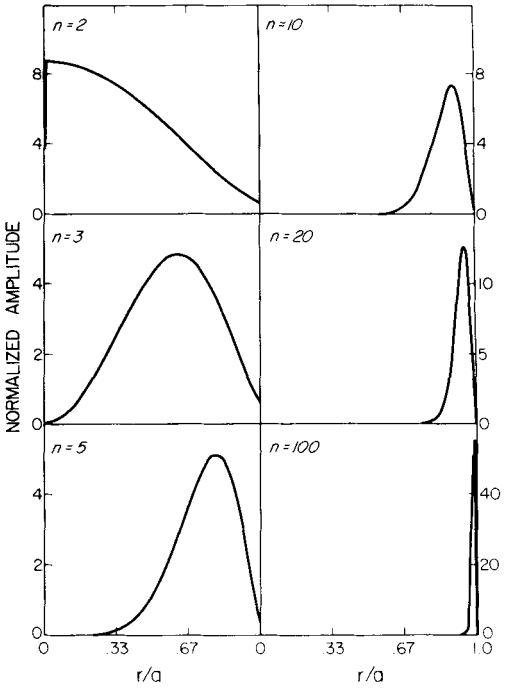

Figure 3. Normalized shear kernels for representative modes of the homogeneous earth model A whose properties are shown in Fig. 4. The angular order n of the mode is shown in each frame. Note that the higher order modes have their shear energies progressively more sharply confined to the near surface region.

In Fig. 3 we show plots of the differential kernel $K(r)$ for a few values of the angular order n. For small values of n (2 and 3) we see that the shear energy in the mode is distributed throughout the Earth's volume while as n increases it becomes progressively more highly concentrated at the Earth's surface.

For this homogeneous earth model the calculation of the residues r_i^n which are required to invert the Love number spectra into the time domain is particularly simple. Since there is only one relaxation time for each value of n we may use equation (55) to obtain

$$r^n = s^n(h_n^\infty - h_n^E) \tag{70}$$

and the complete time domain solution to the inhomogeneous problem may be constructed using (56).

4.3 RELAXATION SPECTRUM FOR A COMPRESSIBLE HOMOGENEOUS EARTH

For the homogeneous compressible model discussed in Section 3.2 we may also compute the eigenspectrum by finding the zeros of a secular determinant which is analogous to that shown explicitly in (31c) for the incompressible problem. Now, however, from (43), the elements of the secular determinant consist of spherical Bessel functions and this introduces a slight complication because the eigenvalues s_j^n are located on the negative real axis of the complex s-plane where the arguments of the Bessel functions may become complex. This may be seen by direct substitution of (3a, b) into equations (41a, b) to give

$$k^2(s) = \frac{2\rho_0 g_0(s + \mu/\nu)}{r(\beta s + K\mu/\nu)}\left[1 + \sqrt{1 + \frac{n(n+1)(\beta s + K\mu/\nu)}{4s\mu}}\right] \tag{71a}$$

$$q^2(s) = \frac{2\rho_0 g_0(s + \mu/\nu)}{r(\beta s + K\mu/\nu)}\left[1 - \sqrt{1 + \frac{n(n+1)(\beta s + K\mu/\nu)}{4s\mu}}\right] \tag{71b}$$

in which $\beta = \lambda + 2\mu$ and $K = \lambda + 2\mu/3$.

There are now five distinct cases which must be treated separately and these are

(1) $s > 0$, in which case $k^2 > 0, q^2 < 0$ and therefore q is purely imaginary.

(2) $s < -\mu/\nu$, then $k^2 > 0$, $q^2 < 0$ and again q is purely imaginary. Here the analysis proceeds in the way pointed out by Gilbert & Backus (1968). We define $p^2 = -q^2$ and find a second solution vector to supplement (43) by substituting $l_n(pr)$ in place of $j_n(kr)$ where l_n is the modified Bessel function.

(3) $-\mu/\nu < s < -(K/\beta)(\mu/\nu)$, in this case $k^2 < 0$ and $q^2 > 0$ so that k is purely imaginary. The appropriate solution vector which replaces (43) then has $j_n(kr)$ replaced by $l_n(pr)$ where $p^2 = -k^2$.

(4) $-(K/\beta)(\mu/\nu) < s < -[n(n+1)K\mu/\nu]/[4\mu + n(n+1)\beta]$, then $k^2 > 0$ and $q^2 > 0$ and the solutions are as before.

(5) $-[n(n+1)K\mu/\nu]/[4\mu + n(n+1)\beta] < s < 0$, in this case k^2 is complex and q is the complex conjugate of k. Therefore $j_n(kr)$ and $j_n(qr)$ are also complex conjugates and this implies that the solution vectors $\mathbf{y}_1$ and $\mathbf{y}_2$ are also. At first sight it therefore appears that in this range of s values there are only two linearly independent solution vectors $\mathbf{y}_1$ and $\mathbf{y}_3$ to satisfy three boundary conditions. However, this is only apparent since the real and imaginary

parts of $\mathbf{y}_1$ are linearly independent. Writing

$$\mathbf{y}_4 = \frac{1}{2}(\mathbf{y}_1 + \mathbf{y}_2) = \mathrm{Re}(\mathbf{y}_1)$$

and

$$\mathbf{y}_5 = \frac{i}{2}(\mathbf{y}_2 - \mathbf{y}_1) = \mathrm{Im}(\mathbf{y}_1)$$

we therefore have a general solution $\mathbf{y} = c_4\mathbf{y}_4 + c_5\mathbf{y}_5 + c_3\mathbf{y}_3$ and the matrix M whose determinant gives the secular function can now be constructed.

No simple analytic expression exists for the eigenvalues s_n in this case and numerical root finding algorithms must be employed. For all of the calculations in this paper where the evaluation of spherical Bessel functions is required, they have been generated using the method of continued fractions. Lentz (1976) has shown this method to be highly efficient, accurate and stable, even for complex arguments. Derivatives of the Bessel functions required in (43) are obtained using the recursion relations. Some eigenvalues for the compressible model are listed in Table 5 where they are compared to their incompressible counterparts. Inspection of this table shows that the effect of compressibility is to shift the eigenvalues to somewhat longer relaxation time but the magnitude of this shift is extremely small.

4.4 RELAXATION SPECTRA ILLUSTRATING SPECIFIC PHYSICAL EFFECTS OF EARTH-LIKE CHARACTERISTICS OF THE VISCOELASTIC MODEL

In this section we shall consider five simple incompressible earth models which have been constructed to illustrate the effects upon the relaxation spectrum of important physical properties of realistic earth models when these properties are isolated from one another. The structure of these models is shown in Fig. 4 where the profiles of $p_0(r)$, $V_S(r)$ and $\nu(r)$ are illustrated. Model A is the homogeneous model discussed previously, B has a 120 km thick lithosphere, C has an inviscid fluid core of radius 3485.5 km and high density contrast, D has an outer shell of thickness 195.6 km in which the density is reduced, while E has high viscosity below a depth of 671 km. The last model F has a *low* viscosity region in the outermost 120 km.

The relaxation spectrum for model B is shown in Fig. 2(b) and may be compared to that for the homogeneous model in Fig. 2(a). Each harmonic of angular order n now has two different modes of relaxation which are accessible to it which we have named M0 for the fundamental mantle mode and L0 for the lithospheric mode. The modes have been identified

Table 5. The effect of compressibility on the eigenvalues $\bar{s}^n$ for a homogeneous earth model.

n	Incompressible	Compressible	Percentage difference
2	−0.9165	−0.9117	0.5
4	−0.7196	−0.7133	0.8
6	−0.5766	−0.5712	0.9
8	−0.4784	−0.4740	0.9
10	−0.4080	−0.4045	1.0
20	−0.2339	−0.2325	0.8
50	−0.1023	−0.1019	0.3

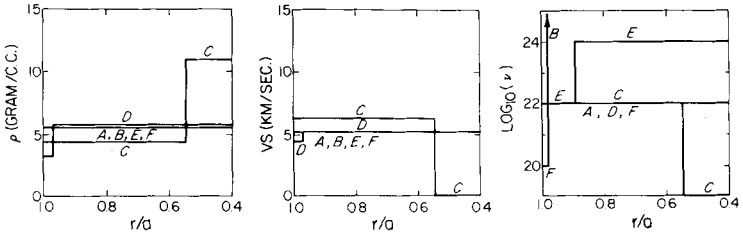

Figure 4. Density (ρ), shear wave velocity (VS), and Newtonian viscosity (ν) for the simple incompressible earth models discussed in the text.

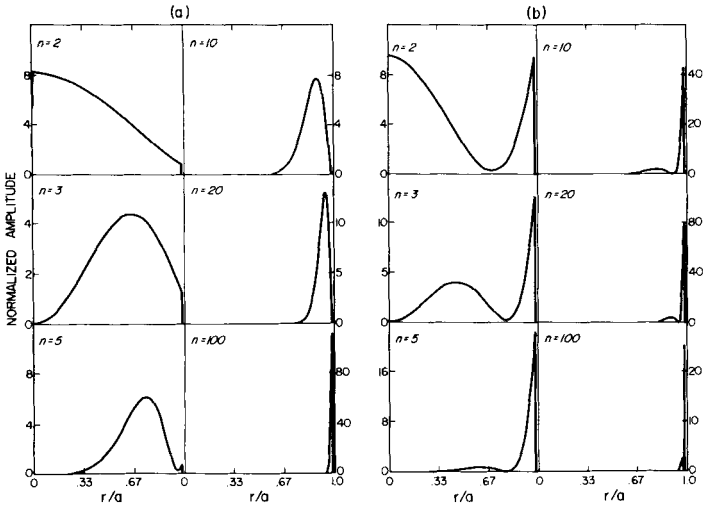

Figure 5. (a) shows normalized shear kernels for a sequence of modes of model B whose angular orders n are marked in each frame. These modes are all along the M0 branch. Corresponding modes along the L0 branch are shown in (b).

by inspection of their shear kernels which are shown for several values of n in Fig. 5(a, b). For modes along the L0 branch, shear energy is concentrated at the base of the lithosphere while for the M0 modes the peak is in the mantle as for the homogeneous models, the kernels for which were illustrated in Fig. 5. Residues for the Laurent series expansions (55) of the solution to the inhomogeneous boundary value problem are listed for this model in Table 6 where we list s_i^n, r_i^n/s_i^n and a percentage strength for each mode as the ratio

$$(r_i^n/s_i^n)/\sum_i (r_i^n/s_i^n).$$

The sum in the denominator in this expression for percentage strength is just the total viscous contribution to the infinite time response. Inspection of this table clearly shows that the L0 modes carry an extremely small fraction of the total variance except near the angular degree n at which the two modal branches cross. The introduction of this extra mode of relaxation is not therefore the most important effect upon the relaxation spectrum which the presence of the lithosphere produces. More important is the fact, evident in Fig. 2(b), that the relaxation times along the M0 branch are sharply reduced at large angular order (short wavelength). Rather than decreasing indefinitely, however, the relaxation time approaches an asymptotic value for large n, the same asymptote as is obtained for the L0 mode. When these two modal

Table 6. Distribution of modal excitation strengths for model B.

	Angular order	M0 branch	L0 branch	Non-elastic amplitude $\Sigma(r_i/s_i)$
s_i		0.9610	0.3523	
r_i/s_i	2	−1.2525	−0.0098	−1.2623
Strength (per cent)		99.2	0.8	
s_i		0.8492	0.5049	
r_i/s_i	3	−1.8024	−0.0324	−1.8348
Strength (per cent)		98.3	1.7	
s_i		0.6474	0.7866	
r_i/s_i	5	−2.7357	−0.3009	−3.0366
Strength (per cent)		90.0	10.0	
s_i		0.4191	1.2575	
r_i/s_i	10	−6.0719	−0.0220	−6.0939
Strength (per cent)		99.7	0.3	
s_i		0.2721	1.8024	
r_i/s_i	20	−10.5121	−0.1583	−10.6704
Strength (per cent)		98.5	1.5	
s_i		1.4861	2.2863	
r_i/s_i	100	−0.6145	−0.0003	−0.6148
Strength (per cent)		100.0	0.0	

lines coalesce, the residues along the M0 branch also go to zero (Table 6) which is simply a mathematical manifestation of the physically intuitive result noted previously that for sufficiently short wavelengths all viscous gravitational relaxation is suppressed by a lithosphere with infinite viscosity. The value of n above which relaxation time first begins to decrease with n is determined by lithospheric thickness. The greater the lithospheric thickness the smaller the value of n at which its presence is felt. In his analysis of the rebound data from Fennoscandia McConnell (1965, 1968) noted this characteristic behaviour and used it to determine a lithosphere thickness of about 120 km for that region.

Fig. 2(c) shows the relaxation diagram for model C which has an inviscid high density core but no lithosphere. Again, the introduction of a second layer into the model (this time with an expression in terms of viscosity *and* density rather than in viscosity only) supports a second mode of relaxation for each angular order of the deformation. Shear kernels along the two modal branches are shown in Fig. 6(a, b) and the branch with longest relaxation times has been labelled C0 on Fig. 2(c). The reason for this is clear from Fig. 6(b) in which the shear kernels are observed to peak adjacent to the core–mantle boundary, identifying the modes as core modes, the family of which we denote as C0. Comparison of Fig. 2(c) with 2(a) shows that the presence of the core has slightly reduced the relaxation times of the mantle modes which have low angular order (large wavelength). For large angular order, both modes have relaxation time increasing with n according to the half-space formula (63). The residues along the M0 and C0 branches are listed in Table 7 for a few n values and show that the relative strength of the relaxation along the C0 branch tends to zero as n increases such that for $n \gtrsim 10$ the presence of the core is no longer felt and the relaxation is governed entirely by the M0 modes. Comparison of the C0 and M0 kernels in Fig. 6 for $n = 100$ shows that they are identical. This is simply a numerical artefact of the fact seen in Fig. 2(c) that the two modal branches coalesce for large n in this model.

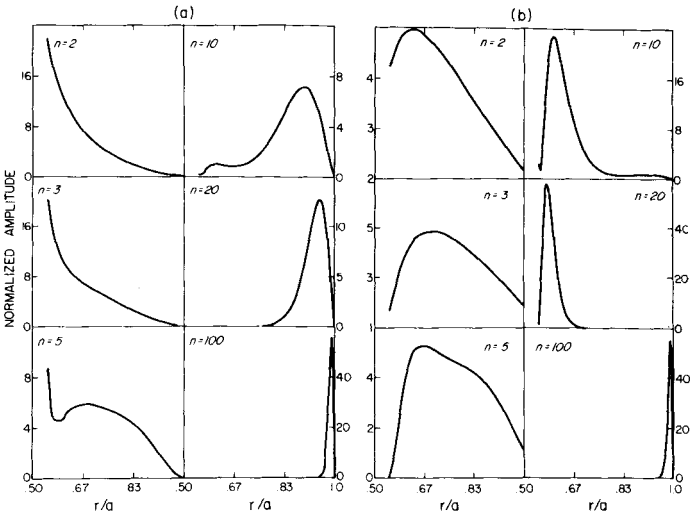

Figure 6. Normalized shear kernels for model C with angular orders shown in each frame. Those shown in (a) are along the M0 branch whereas those shown in (b) are along the C0 branch.

The relaxation diagram for model D is shown in Fig. 2(d). This model has an upper mantle density jump which is not accompanied by any change of viscosity but has neither core nor lithosphere. It is intended to mimic the effect of density jumps introduced by phase changes in the transition region. As seen in Fig. 2(d) such a feature again introduces a second mode of relaxation for each angular order n. The new modes are labelled M1 in the figure

Table 7. Distribution of modal excitation strengths for model C.

	Angular order l	C0 branch	M0 branch	Non-elastic amplitude $\Sigma(r_i/s_i)$
s_i		0.4099	2.2158	
r_i/s_i	2	−0.9065	−0.6489	−1.5554
Strength (per cent)		58	41	
s_i		0.4233	1.5250	
r_i/s_i	3	−1.2566	−1.1079	−2.3645
Strength (per cent)		53	47	
s_i		0.4241	0.7613	
r_i/s_i	5	−1.8347	−2.2059	−4.0406
Strength (per cent)		45	55	
s_i		0.3151	0.3515	
r_i/s_i	10	−0.5030	−7.6242	−8.1272
Strength (per cent)		6	94	
s_i		0.1738	0.1947	
r_i/s_i	20	−0.0113	−16.3348	−16.3461
Strength (per cent)		0	100	
s_i		0.0376	0.0428	
r_i/s_i	100	−0.0110	−82.4318	−82.4429
Strength (per cent)		0	100	

and for all n have longer relaxation times than for those along the M0 branch. With the large density jump in model D, the M1 mode can carry as much as 49 per cent of the relaxation in the modes with small angular order. For $n \gtrsim 60$, however, the M1 mode becomes less important and the M0 modes dominate once more. The modes labelled T1 and T2 are spurious in the sense that they are not excited by surface loading.

Fig. 2(e) shows the relaxation diagram for model E and this demonstrates that the effect of increasing the viscosity of the lower mantle is to increase the relaxation times for those long-wavelength harmonics which involve this region in their decay.

The relaxation diagram for the last model F which includes a low viscosity zone extending to the planet's surface is shown in Fig. 2(f). For large angular order ($n \gtrsim 150$), the relaxation times fit the half-space formula (63) with ν equal to the viscosity of the low viscosity upper mantle. For small angular order ($n \lesssim 4$) the relaxation times are those given by the homogeneous model A perturbed slightly to shorter times. For intermediate values of the angular order, the M0 branch turns towards shorter relaxation times, the same effect which we noted earlier as being produced by the presence of a lithosphere. This points out an important ambiguity in the interpretation of observed relaxation spectra. Both low and high near-surface viscosity effect a spectrum characterized by decreasing relaxation time with increasing wavenumber.

4.5 RELAXATION SPECTRA FOR REALISTIC EARTH MODELS

In this section we shall describe relaxation spectra for three compressible realistic earth models whose elastic properties and density are the same as those in model 1066B of Gilbert & Dziewonski (1975). Plots of these properties are shown in Fig. 7, prominent features of which are the presence of the solid inner core and the existence of three sharp density discontinuities in the upper mantle corresponding (in the order of increasing depth) to: (1) the Mohorovičić discontinuity, (2) the olivine → spinel phase change, and (3) the spinel → post-spinel phase change. Included in Fig. 7(b) are the viscosity profiles which are required to complete the specification of the viscoelastic models. Model L1 has a 120 km thick lithosphere, a mantle with a constant viscosity of 10^{22} P and inviscid core; L2 is the same but with a lower mantle viscosity of 10^{23} P, while L3 is the same as L2 but includes a low viscosity zone beneath the lithosphere which is 10^2 km thick and in which the viscosity is 10^{20} P.

The relaxation spectra calculated for these models have all been obtained using the compressible field equations. In Fig. 8 we show the secular determinant for model L1 at angular order $n = 6$ as an illustration. Not all the roots of this transcendental function are physically significant but those that are plotted in Fig. 9(a) are members of six prominent modal branches labelled M0, M1, M2, C0, C1, L0. The C1 branch is due to the presence of the inner core, as can be seen by inspection of the shear kernels for this model, but exerts negligible influence upon the relaxation as can be seen by inspection of relative relaxation strengths listed in Table 8. The M1 and M2 branches are due to the density discontinuities at 671 and 420 km depths respectively. Inspection of Table 8 shows that M1 is more important to the relaxation than M2 and this is because the density jump across 671 km is about double that across 420 km. The rest of the relaxation diagram is self-explanatory on the basis of the results discussed in the last subsection. The C0 modes are due to the core and carry about 40 per cent of the viscous relaxation at $n = 2$ and about 4 per cent at $n = 6$. The L0 modes are due to the presence of the lithosphere and do not participate substantially in the relaxation. The M0 modes are most important and carry more than 90 per cent of the relaxation for $n \gtrsim 15$. The turning of the M0 branch to shorter relaxation times is due to the presence of the lithosphere.

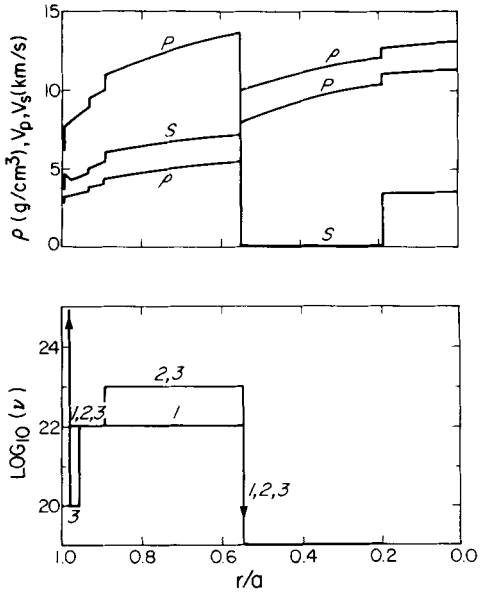

Figure 7. The elastic structure for all of our 'realistic' earth models is that shown in the upper diagram. The density, compressional, and shear wave velocity profiles are for model 1066B of Gilbert & Dziewonski (1975). The viscosity profiles for models L1, L2 and L3 are shown in the lower diagram where they are denoted 1, 2 and 3 respectively.

The relaxation diagram for model L2 is shown in Fig. 9(b) and inspection reveals all of the modal branches found for model L1 although some of these have been considerably modified in form. The effect of the 10^{23} P lower mantle is seen to increase the relaxation times of both C0 and C1 by an order of magnitude. The relaxation times along the M0 branch for $n \lesssim 20$ and along the M1 branch for $n \gtrsim 20$ are affected likewise. The M2 branch

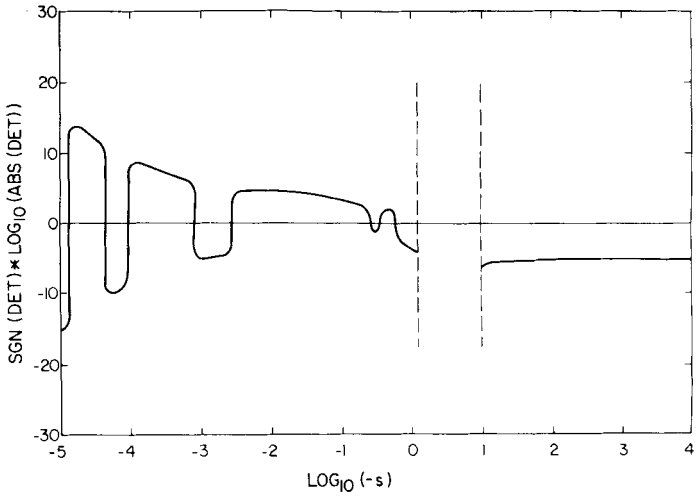

Figure 8. The secular determinant for realistic earth model L1 as a function of inverse relaxation time $s = \tau^{-1}$ and for angular order $n = 6$. The zeros of the secular function determine the discrete spectrum of decay times for each of the normal modes of viscous gravitational relaxation with $n = 6$. Between the dashed lines exists a sequence of interlaced singularities and non-physical zeros.

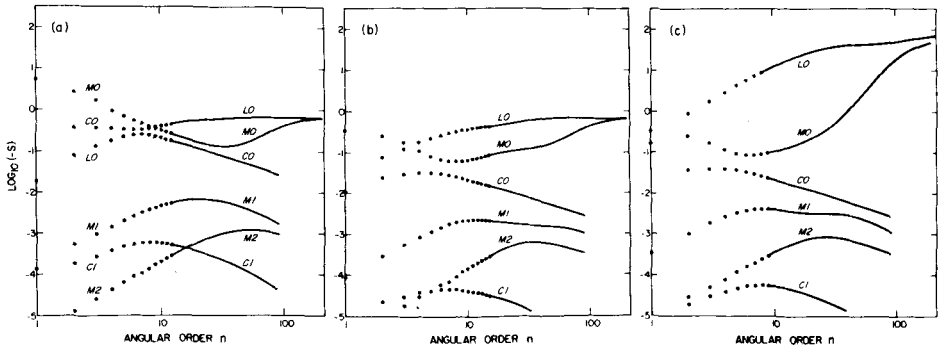

Figure 9. Relaxation diagrams for the three realistic earth models L1, L2 and L3 are shown respectively in (a), (b) and (c).

is modified only slightly except in the range $20 \lesssim n \lesssim 50$. Along the lithosphere branch the modes with $n \lesssim 20$ show strong interaction with the mantle modes (as evidenced by the shear kernels) and now carry a significant fraction of the total viscous relaxation. The high viscosity lower mantle also tends to suppress the importance of the C0 mode for $n \lesssim 4$ but accentuates its importance for $4 \lesssim n < 9$. The M0 branch is still dominant for

Table 8. Modal excitation strengths for model L1.

	n	M0	M1	M2	C0	L0	$-\Sigma r_i/s_i$
s_i		2.7632	0.00053	0.00001	0.3746	0.0782	
r_i/s_i	2	−0.7327	−0.3822		−0.7431		1.8579
Strength (per cent)		40	20		40		
s_i		0.9671	0.00144	0.00004	0.3683	0.1837	
r_i/s_i	4	−2.7216	−0.7695		−0.5840		4.0751
Strength (per cent)		67	19		14		
s_i		0.5698	0.00262	0.00009	0.3404	0.2563	
r_i/s_i	6	−5.0863	−0.9005		−0.2760		6.2627
Strength (per cent)		81	14		5		
s_i		0.4135	0.00379	0.00014	0.2503	0.3617	
r_i/s_i	8	−7.4537	−0.9388				8.3926
Strength (per cent)		89	11				
s_i		0.3244	0.00473	0.00021	0.2140	0.4164	
r_i/s_i	10	−8.0725	−1.1263	−0.0439		−1.2578	10.5004
Strength (per cent)		76.9	10.7	0.4		12	
s_i		0.2178	0.00629	0.00040	0.1520	0.5152	
r_i/s_i	15	−14.0049	−1.0892	−0.1126		−0.3441	15.5507
Strength (per cent)		90	7	0.7		2.3	
s_i		0.1668	0.00679	0.00061	0.1176	0.5818	
r_i/s_i	20	−18.5911	−0.8604	−0.1310		−0.2174	19.799
Strength (per cent)		94	4.3	0.7		1	
s_i		0.1709	0.00387	0.00125	0.0499	0.6982	
r_i/s_i	50	−14.5539	−0.0329			−0.0595	14.6463
Strength (per cent)		99.3	0.2			0.5	
s_i		0.4466					
r_i/s_i	100	−2.2162					2.2162
Strength (per cent)		100					

$n \gtrsim 8$ as will be clear by inspection of Table 9 which shows relative relaxation strength for all modes belonging to each of several angular orders.

In Fig. 9(c) is shown the relaxation diagram for model L3 which differs from L2 only in the presence of a low viscosity zone beneath the lithosphere. The branches M0, M1, M2, C0, C1 have the same origin as in the last models but here the branch L0 represents a combined effect due both to the lithosphere and to the low viscosity channel. Comparing this relaxation diagram with that for model L2 shown in Fig. 9(b) we see that the relaxation times of the C0 and C1 modes have been shifted very slightly towards shorter times. The M1 and M2 branches are shifted more strongly in this direction and the lower the angular order the larger the shift. Along the M0 branch, the effect of the low viscosity zone is to decrease the relaxation time with n even more sharply than it previously varied due to the presence of the lithosphere alone. Inspection of the shear kernels along this branch shows that for $n \gtrsim 50$ the M0 branch begins to lose its dominance as L0 begins to carry a significant fraction of the total relaxation. Finally for sufficiently large n ($\gtrsim 150$) the two branches cross and M0 again dominates the relaxation.

In Fig. 10 we show a superposition of the M0 modes for all of the previously discussed models and for a fourth model L4 which is identical to L3 except that the low viscosity channel has a viscosity of 10^{21} P rather than 10^{20} P. Also shown on this diagram are several observational data points. These include different estimates of the relaxation time for the

Table 9. Modal excitation strengths for model L2.

	n	M0	M1	M2	C0	L0	$-\Sigma r_i/s_i$
s_i		0.2571	0.00029	0.00001	0.0244	0.0762	
r_i/s_i	2	−0.8211	−0.2630	−0.0835	−0.5629	−0.1272	1.85797
Strength (per cent)		44.3	14.2	4.5	30	6.8	
s_i		0.1102	0.00085	0.00003	0.0320	0.1784	
r_i/s_i	4	−1.0083	−0.4621	−0.1216	−1.0679	−1.4153	4.0751
Strength (per cent)		24.7	11.3	3	26.2	34.7	
s_i		0.0676	0.00147	0.00006	0.0307	0.2665	
r_i/s_i	6	−3.5416	−0.4893	−0.1792	−0.8250	−1.2277	6.2627
Strength (per cent)		56.6	7.8	2.8	13.2	19.6	
s_i		0.0612	0.00197	0.00010	0.02580	0.3281	
r_i/s_i	8	−5.8899	−0.3879	−0.2181	−0.4489	−1.4480	8.3926
Strength (per cent)		70.2	4.6	2.5	5.3	17.3	
s_i		0.0647	0.0020	0.00014	0.0219	0.3651	
r_i/s_i	10	−8.2332	−0.6430			−1.6242	10.5004
Strength (per cent)		78.4	6.1			15.5	
s_i		0.0849	0.00215	0.00028	0.0152	0.4340	
r_i/s_i	15	−13.4477	−0.4637			−1.6393	15.5507
Strength (per cent)		86	3			11	
s_i		0.1029	0.00190	0.00043	0.0118	0.4847	
r_i/s_i	20	−18.3252	−0.3821			−1.0926	19.7999
Strength (per cent)		93	2			5	
s_i		0.1703	0.00156	0.00055	0.0050	0.6917	
r_i/s_i	50	−14.6463					14.6463
Strength (per cent)		100					
s_i		0.4466					
r_i/s_i	100	−2.2162					2.2162
Strength (per cent)		100					

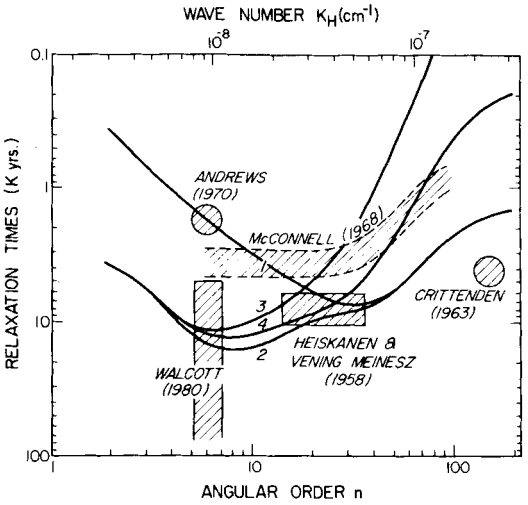

Figure 10. Solid lines illustrate the variation of relaxation time with horizontal wavenumber k_H (or angular order n) for the realistic earth models L1, L2, L3 and L4 which are discussed in the text. Each model is described by the relaxation times which obtain along the M0 branch of the modal diagram. Model L4 differs from L3 only in that the low viscosity channel has a viscosity of 10^{21} P rather than the 10^{20} P which is obtained for L3. Also shown are the relaxation times observed by various authors in different wavenumber regimes.

central Laurentide depression. Based on sea-level data from the Ottawa Islands, Andrews (1970) obtained a relaxation time of approximately 2000 yr. However, Walcott (1980) argued for relaxation times in excess of 5000 yr. His argument was based upon the large gravity anomaly observed over central Hudson Bay and sea-level data from Castle Island and Cape Henrietta Maria in south-eastern Hudson Bay. We have assigned these relaxation times to angular order $n = 6$ on the basis that this is the dominant harmonic in the decomposition of the Laurentide ice sheet (Peltier & Andrews 1976). Also shown in the figure is Crittenden's (1963) estimate of 4000 yr for the relaxation time of Pleistocene Lake Bonneville. Heiskanen and Vening-Meinesz estimate of a relaxation time of 5000 yr for the Fennoscandian depression is also included. Superimposed upon these single estimates is the broad spectrum of relaxation times inferred by McConnell (1968) from a deconvolution of cross-sectional data from Fennoscandia. His estimates extend over the range of angular orders $5 \lesssim n \lesssim 100$ but are liable to be extremely inaccurate at both the long- and short-wavelength ends. They do, however, show quite unambiguously the decrease of relaxation time with increasing n which indicates the presence of a lithosphere, a low-viscosity zone or a combination of both.

On the basis of this comparison one may be rather strongly inclined to state that model L1 is preferred since the models with high lower mantle viscosity are very strongly rejected by the Laurentide data. This, of course, assumes that Andrews' estimate and not Walcott's is most representative of the relaxation at the centre of the Laurentide depression. Similarly, the models with sharp low-viscosity zones seem to be rejected by the Lake Bonneville observation since they predict far too rapid a decrease of relaxation time with increasing angular order. This conclusion may be somewhat premature, however, since the comparisons upon which it is based are themselves predicated upon the assumption that only the M0 mode is significant in determining the relaxation of a harmonic surface deformation of any angular order. Results discussed previously in this section demonstrate that this assumption is not strictly true. The only way to remove the ambiguity of interpretation which is intro-

duced in the inversion of data using a realistic viscoelastic earth model which supports a multiplicity of normal modes of viscous gravitational relaxation for each angular order n is to use the model to make direct predictions of the surface observables themselves. These observables include relative sea-level histories and present-day free air gravity anomalies. In the next section we will illustrate further elaborations of the theory which are required to make such predictions.

5 Viscoelastic response to the growth and decay of a model ice sheet

In order to determine the response of the viscoelastic earth to surface loading by a specific space-time loading event we are obliged first to determine the response to the point load by summing infinite series such as (5). The response to an arbitrary loading event may then be determined by superposition (convolution). Prior to summing the series in (5) we express the spectral amplitudes U_n, V_n, Φ_n in terms of surface load Love numbers through (12). We showed previously using the normal mode formalism that when the surface load had a $\delta(t)$ time dependence the Love numbers $h_n(t)$, $l_n(t)$, $k_n(t)$ all had expansions of the form

$$h_n(t) = h_n^{\mathrm{E}}\delta(t) + \sum_j r_j^n \exp(-s_j^n t)\,. \tag{72}$$

If the point load is applied at $t = 0$ and then allowed to remain on the surface, i.e. has a Heaviside history, then the induced deformation can be calculated using Love numbers obtained from (72) by convolution with a unit step. Denoting these Love numbers by $h_n^{\mathrm{H}}(t)$, etc., we obtain

$$h_n^{\mathrm{H}}(t) = h_n^{\mathrm{E}} + \sum_j \frac{r_j^n}{s_j^n}\left[1 - \exp(-s_j^n t)\right]. \tag{73}$$

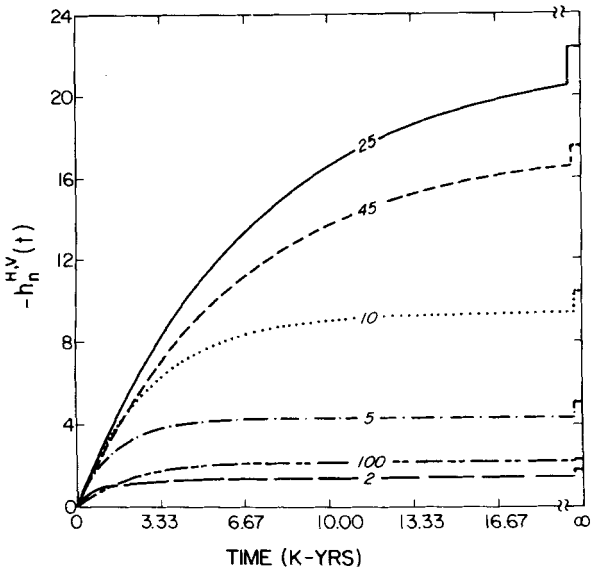

Figure 11. Decay spectra $h_n^{H,V}(t)$ for realistic earth model L1. The angular order n is marked on each decay curve and time is measured in thousands of years. The asymptotic value which is obtained at infinite time is shown for each n adjacent to the right hand margin of the graph. Note that even after 2×10^4 yr substantial disequilibrium remains for most angular orders.

In Peltier (1976) the second term on the rhs was denoted by $h_n^{H,V}(t)$, the viscous part of the Heaviside response, and in Fig. 11 we show histories $h_n^{H,V}(t)$ for several values of the angular order n. These time domain forms are for model L1 discussed in the last section. The symbols on the right margin in Fig. 11 show the infinite time asymptotes

$$\sum_j r_j^n / s_j^n$$

which may be calculated exactly by solving the second-order system of o.d.e.'s discussed in Section 3.3. As we shall see below, having accurate values of the infinite time Love numbers is crucial for calculation of the gravity anomaly.

Green's functions for the Heaviside response are obtained by using forms like (73) for the Love numbers in (12) and then summing infinite series of the form (5). We may calculate Green's functions for several signatures of the response, and all of these may be written as the sum of two parts as

$$G^H(\theta,t) = G^E(\theta) + G^{H,V}(\theta,t). \tag{74}$$

Here we shall be concerned only with the Green's functions for radial displacement and free air gravity anomaly which we shall denote by u^H and g^H respectively and which have the forms

$$u^H(\theta,t) = \frac{a}{m_e}\sum_{n=0}^{\infty} h_n^E P_n(\cos\theta) + \frac{a}{m_e}\sum_{n=0}^{\infty} h_n^{H,V}(t) P_n(\cos\theta) \tag{75a}$$

$$g^H(\theta,t) = \frac{g}{m_e}\sum_{n=0}^{\infty}[n + 2h_n^E - (n+1)k_n^E]\,P_n(\cos\theta)$$

$$+ \frac{g}{m_e}\sum_{n=0}^{\infty}[2h_n^{H,V}(t) - (n+1)k_n^{H,V}(t)P_n(\cos\theta)]\,. \tag{75b}$$

Figs 12, 13 and 14 respectively show the $u^{H,V}(\theta,t)$ part of the radial displacement Green's function for models L1, L2 and L3 discussed in the last section. All functions in these presentations have been normalized by multiplication with $(a\theta)$ for plotting purposes. The absence of a singularity 'stronger' than $(a\theta)$ at $\theta = 0$ is due to the presence of the lithosphere. As discussed in Peltier (1974) the most diagnostic feature present in the Green functions themselves, aside from the variation of the rate of decay in the small θ region, is the behaviour of the peripheral bulge. The uniform viscosity mantle supports an inward propagating forebulge (Fig. 12) and the inward migration is accompanied by an increase in both width and amplitude of this peripheral region. For model L2, which has a high viscosity lower mantle, inspection of Fig. 13 shows that the bulge does not migrate nor does its width change. The amplitude of the bulge, however, increases more rapidly than for the uniform mantle model. The effect of a low viscosity zone on the Green functions (model L3, Fig. 14) is to cause the bulge to migrate outwards – the opposite of the sense of motion in the uniform mantle case.

By convolving Green's functions (74) over a realistic space–time deglaciation history one may obtain a prediction of the Earth's response to such an event. Here we shall restrict consideration to ice loads with simple geometric forms which may nevertheless serve as useful approximations to actual unloading events. The first model we shall discuss is one in which the ice sheet is approximated as a disc load of radius α. Let O be the centre of the disc and Q be a point of observation *outside* the disc load with Γ the angular distance between O and

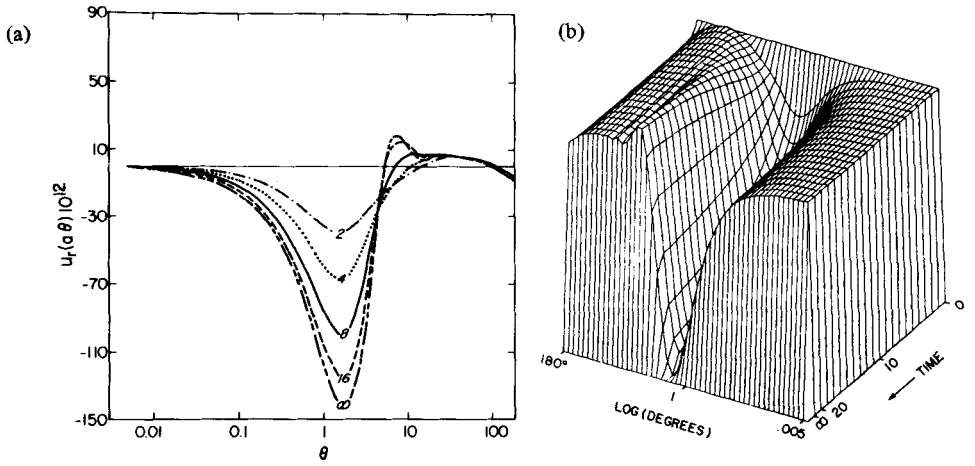

Figure 12. (a) shows several time slices through the viscous part of the Heaviside Green's function for radial displacement for model L1. The function has been normalized by multiplication with $a\theta$ to remove the geometric singularity for plotting purposes. The number on each curve is time measured in thousands of years. Note the inward migration of the peripheral bulge as time proceeds for this uniform viscosity model. (b) shows a three-dimensional view of the same Green's function.

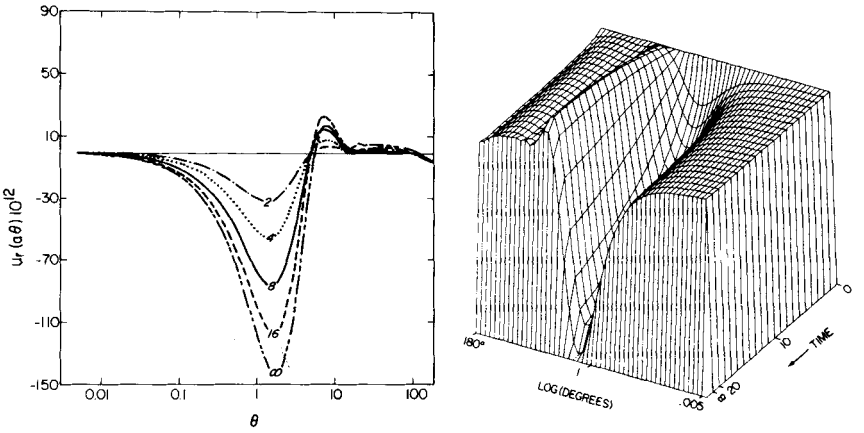

Figure 13. Same as Fig. 12 but for viscoelastic model L2. Note the stationary nature of the collapsing peripheral bulge for this model which has a high lower mantle viscosity.

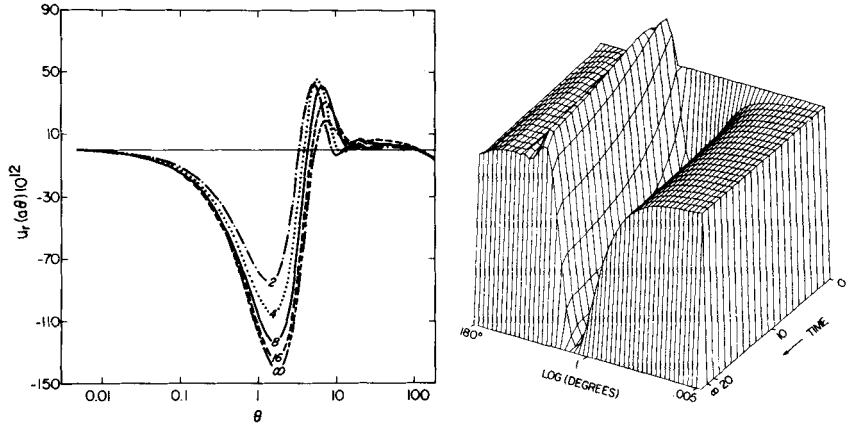

Figure 14. Same as Fig. 12 but for viscoelastic model L3. Note that the peripheral bulge migrates outwards prior to its collapse.

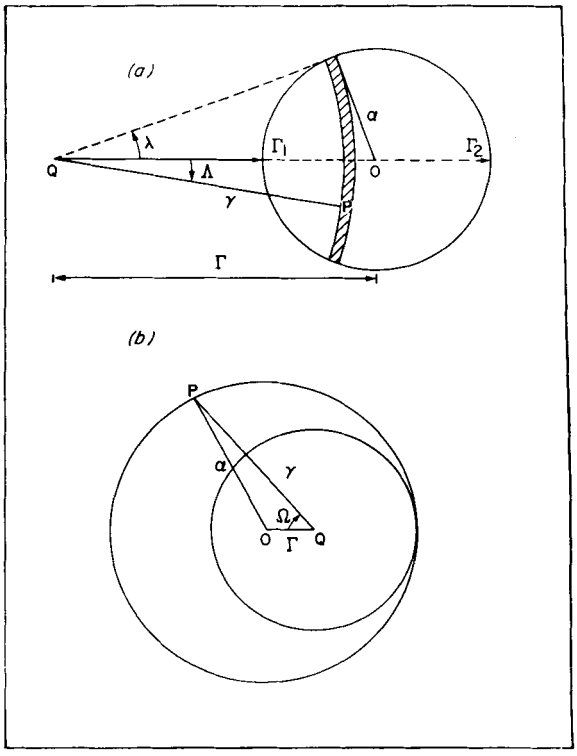

Figure 15. (a) Notation employed for the calculation of the response at point Q outside a circular disc of radius α. (b) Illustrates the setup of the problem when the point of observation is inside the disc.

Q (see Fig. 15a). Any point P on the disc may be described by γ, the angular distance from Q, and Λ the angle PQO. Note that γ and Λ are such that $\Gamma_1 \leqslant \gamma \leqslant \Gamma_2$ and $-\lambda(\gamma) \leqslant \Lambda \leqslant \lambda(\gamma)$ where $\Gamma_1 = \Gamma - \alpha$ and $\Gamma_2 = \Gamma + \alpha$. If we denote by E the response at Q due to a disc of mass L, then

$$E(\Gamma,t) = a^2 L \int_{\Gamma_1}^{\Gamma_2} \int_{-\lambda(\gamma)}^{\lambda(\gamma)} G(\gamma,t)\gamma d\gamma d\Lambda \tag{76}$$

where $G(\gamma,t)$ is the Heaviside Green's function and it has been assumed that the disc has been placed on the surface at $t = 0$. Defining a weighting function $W(\gamma)$ as

$$W(\gamma) = \int_{-(\lambda)}^{\lambda(\gamma)} d\Lambda = 2\lambda(\gamma) \tag{77a}$$

then

$$E_{\text{outside}}(\Gamma,t) = a^2 L \int_{\Gamma_1}^{\Gamma_2} G(\gamma,t) W(\gamma)\gamma d\gamma\,. \tag{77b}$$

It is a relatively simple problem in spherical trigonometry to determine $W(\gamma)$ for the disc load. If both α and Γ are much less than the Earth's radius then the geometry is that of a flat

earth and we may use the usual law of cosines to obtain

$$\lambda(\gamma) = \cos^{-1}\left(\frac{\gamma^2 + \Gamma^2 - \alpha^2}{2\gamma\Gamma}\right) \tag{78}$$

for $\Gamma - \alpha \leqslant \gamma \leqslant \Gamma + \alpha$ and $\lambda(\gamma)$ defines the boundary of the disc. If Γ or α are large, however, then we must employ the spherical law of cosines which gives

$$\cos\alpha = \cos\Gamma\cos\gamma + \sin\Gamma\sin\gamma\cos\lambda(\gamma) \tag{79}$$

in which case

$$\lambda(\gamma) = \cos^{-1}\left[\frac{\cos\alpha - \cos\Gamma\cos\gamma}{\sin\Gamma\sin\gamma}\right] \tag{80}$$

and the response to the disc is

$$E_{\text{outside}}(\Gamma, t) = 2a^2 L \int_{\Gamma-\alpha}^{\Gamma+\alpha} \lambda(\gamma) G(\gamma, t)\sin\gamma d\gamma\,. \tag{81}$$

For a point of observation *inside* the disc load (i.e. $|\alpha| > |\Gamma|$), the response E may be split into two parts as

$$\begin{aligned} E_{\text{inside}}(\Gamma, t) = &\int_0^{\alpha-\Gamma} (2\pi a^2 L)\sin\gamma G(\gamma, t) d\gamma \\ &+ \int_{\alpha-\Gamma}^{\alpha+\Gamma} (a^2 L) W(\gamma) G(\gamma)\sin\gamma d\gamma\,. \end{aligned} \tag{82}$$

In (82) the first integral represents the response due to a small disc of radius $\alpha - \Gamma$ and centred at Q, whereas the second is the response to the remainder of the disc in which the weighting function is $W(\gamma) = 2\Omega(\gamma)$. From the spherical law of cosines we have (Fig. 15b)

$$\cos\Omega = \frac{\cos\alpha - \cos\gamma\cos\Gamma}{\sin\gamma\sin\Gamma}\,. \tag{83}$$

From the law of cosines we have

$$\cos\left(\frac{\Omega}{2}\right) = \frac{1 + \cos\Omega}{2} \tag{84}$$

so that

$$\Omega = 2\cos^{-1}\left[\frac{\sin\xi\sin(\xi - \alpha)}{\sin\gamma\sin\Gamma}\right]^{1/2} \tag{85}$$

where $\xi = (\alpha + \gamma + \Gamma)/2$. Equation (82) may therefore be written as

$$E_{\text{inside}}(\Gamma, t) = a^2 L \int_0^{\alpha+\Gamma} G(\gamma, t)\,\tilde{W}(\gamma)\sin\gamma d\gamma \tag{86}$$

where

$$\begin{aligned} \tilde{W}(\gamma) &= 2\pi \quad \text{for} \quad 0 \leqslant \gamma \leqslant \alpha - \Gamma \\ &= 4\cos^{-1}\left[\sqrt{\frac{\sin\xi\sin(\xi - \alpha)}{\sin\gamma\sin\Gamma}}\right] \quad \text{for} \quad \alpha - \Gamma \leqslant \gamma \leqslant \alpha + \Gamma\,. \end{aligned} \tag{87}$$

To determine the response of the Earth to a disc load applied on its surface at $t = 0$ we evaluate the integral (81) or the integral (86) depending upon whether the point of observation is inside or outside of the edge of the disc. These simple integrals may be evaluated using Simpson's rule. To calculate the radial displacement induced by the disc load we use equation (75a) for $G(\gamma, t)$ and to calculate the free air gravity anomaly we use (75b).

5.1 RADIAL DISPLACEMENT RESPONSE

In Fig. 16(a,b,c) we show radial displacement response curves for a disc load with radius $\alpha = 15°$ (about Laurentide size) and for earth models L1, L2 and L3 respectively. The surface deflection is shown for the same sequence of times in each of the three cases and the times are themselves given in the figure legends. The extent of the load is shown by the horizontal line at zero radial displacement. It is evident by inspection of this figure that the nature of the bulge which forms peripheral to the ice sheet itself is just that seen previously in Green's functions. Also evident is the fact that the relaxation proceeds more quickly in the central region for model L1 than it does for either model L2 or L3. This is explicable quite simply in terms of the higher viscosity of the lower mantle in both of the latter two models. Also evident in Fig. 16 is the fact that the submergence in response to the addition of the disc load is not monotonic in the central region for model L1. This effect is not caused by a numerical error in the calculation. To see how this occurs we may, using the spherical harmonic expansion (75a) for the radial displacement Green's function, rewrite our previous expression for the response at Q in the form

$$E(\Gamma, t) = \sum_{n=0}^{\infty} h_n^{\mathrm{H}}(t) Q_n(\alpha, \Gamma) \tag{88}$$

where

$$Q_n = \frac{2a^3}{m_e} \int_{\Gamma-\alpha}^{\Gamma+\alpha} \lambda(\gamma) P_n(\cos\gamma) \sin\gamma d\gamma, \qquad \Gamma > \alpha \tag{89}$$

$$= \frac{2a^3}{m_e} \int_{0}^{\alpha+\Gamma} \lambda(\gamma) P_n(\cos\gamma) \sin\gamma d\gamma, \qquad \Gamma \leqslant \alpha .$$

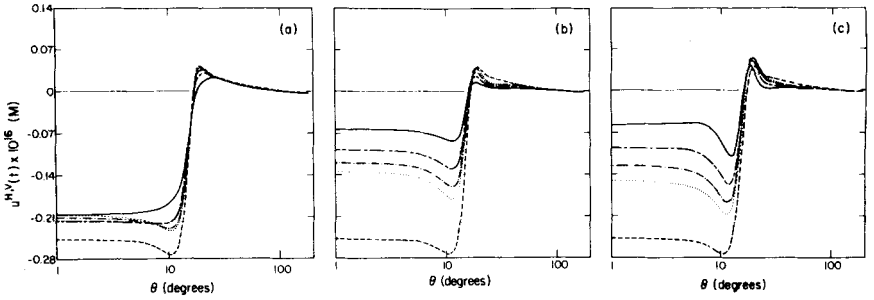

Figure 16. Radial displacement as a function of time and angular distance θ from the centre of a surface disc load of radius $\alpha = 15°$ and mass 1 kg. (a), (b) and (c) are for models L1, L2 and L3 respectively and the times in each frame are denoted by line intensity: ——, $t = 4$ kyr; —— – ——, $t = 8$ kyr; —— · ——; $t = 12$ kyr; ·····, $t = 16$ kyr; ————, $t = \infty$ yr. The horizontal straight line through the origin shows the angular extent of the disc load. Note that the non-monotonic nature of the response for model L1 in the central region is explained in the text. The elastic contribution to the total response is not included on these diagrams.

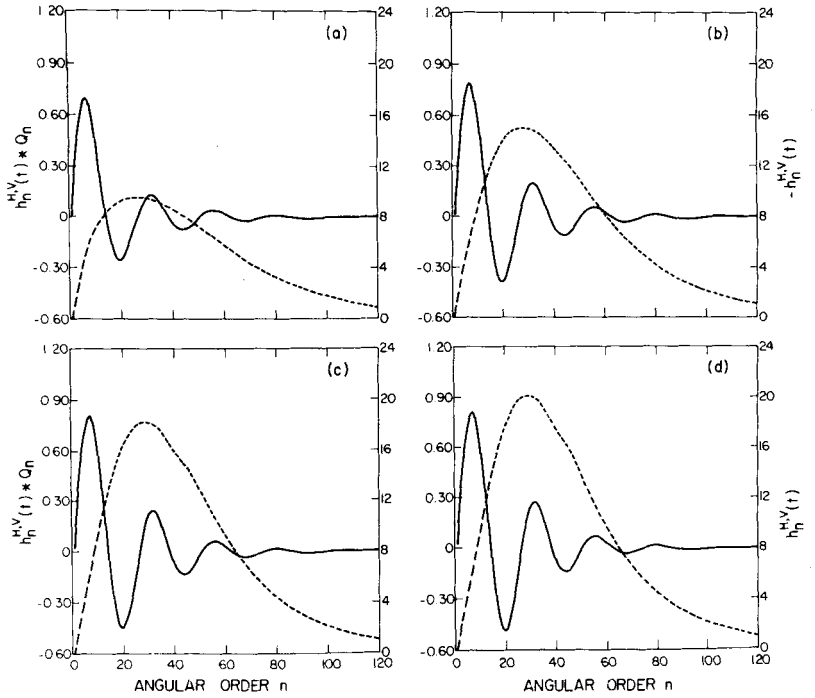

Figure 17. Plots of the Love number $h_n^{H,V}(t)$ (dashed line) and $h_n^{H,V}(t) \cdot Q_n$ (solid line) as a function of angular order n. (a) is for $t = 4$ kyr while (b), (c) and (d) are for $t = 8$, 12 and 16 kyr respectively. The Love numbers $h_n^{H,V}$ are all for model L1.

In Fig. 17 we plot $-h_n^{H,V} Q_n(\alpha, \Gamma)$ (solid curve) and $-h_n^{H,V}(t)$ (dashed curve) as a function of angular order n for several times following application of the load (Fig. 17a, b, c, d). At each time the response may be thought of as equal to the area under the solid curve. For $T \lesssim 8$ kyr the modulus of each term in the series (88) is increasing smoothly. However, since the long-wavelength harmonics in L1 have very short relaxation times, the peak at $n \simeq 6$ (which dominates the harmonic expansion of the disc with radius $\alpha = 15^\circ$) ceases to grow for $8\,\text{kyr} \lesssim t \lesssim 10^2\,\text{kyr}$. In this range of times, though, the minimum in the series $-h_n^H(t) Q_n$ continues to deepen since these angular orders have considerably longer relaxation times as will be seen by reference to the relaxation diagram for this model shown previously in Fig. 11. This is the source of the non-monotonic relaxation under the disc for model L1 which is observed in Fig. 16(a). The only additional feature of interest in these disc load solutions is the fact that the maximum depression is not obtained under the centre of the disc itself but is rather found just inside of the disc edge. This is a consequence of the presence of the lithosphere and of the fact that the disc load has a square edge. As we shall see momentarily, this effect does not occur for ice sheets which have a more realistic parabolic topography.

Solutions for such topographies are shown in Fig. 18(a, b, c) in which parabolic approximations to the Lake Bonneville, Fennoscandia and Laurentide loads have been constructed and all calculations have been performed using viscoelastic model L1. The water load used in the construction of Fig. 18(a) for Lake Bonneville is that estimated by Crittenden (1963) who obtained a maximum depth of the lake of about 305 m corresponding to a mass of approximately 10^{16} kg. Inspection of the calculated response in Fig. 18(a) shows that the maximum amplitude of the response predicted by the model is only about 12 m as compared

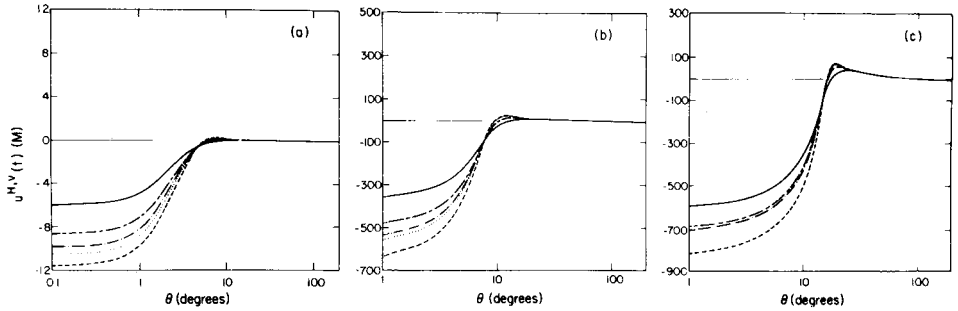

Figure 18. Same as Fig. 16 except for parabolic loads with mass and spatial extents comparable to (a) Lake Bonneville, (b) Fennoscandia, and (c) Laurentide. The viscosity model employed for each calculation is L1. Note that for the parabolic load the response at the centre of the Laurentide ice sheet is now monotonic in time although the rate of sinking is so slow after 12 kyr that it cannot be distinguished from the 16 kyr curve.

to the observed maximum of 64 m. Therefore, although L1 predicts a relaxation time close to the observation, the predicted amplitudes are considerably underestimated. The reason for this is clearly that the lithospheric thickness in L1 is excessive for the basin and range region and this leads to a suppression of the viscous relaxation. If we are to fit the total deflection at this site the lithosphere can be at most 40 km thick. This modification of the model results in a marked increase in the relaxation time for the dominant wavelengths in the response and so must be corrected for by the introduction into the model of a low-viscosity zone in the region immediately beneath the lithosphere.

In the construction of Fig. 18(b,c) for the approximate Fennoscandia and Laurentide scale loads, the parabolic profiles were taken to have maximum thicknesses of 2500 and 3500 m respectively based upon the ice sheet reconstructions in Peltier & Andrews (1976). As shown in Wu & Peltier (1982) which is concerned with detailed comparisons with the observational data, both of these maximum thicknesses are somewhat excessive and so the response amplitudes should not be taken too seriously. The main points to note here are that for the parabolic ice caps the maximum response is obtained at their centres and the displacement in the central region is monotonic in time.

In Fig. 19(a,b,c) we show the 'displacement remaining' at the centre of these parabolic ice sheets as a function of time and for each of the viscosity models L1, L2, L3. The loads are placed on the surface at $t = 0$ and the 'displacement remaining' is calculated as the difference $[u(\theta = 0, t) - u(\theta = 0, \infty)]$ between the instantaneous radial displacement and that

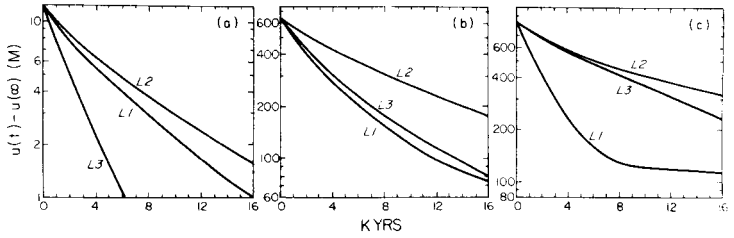

Figure 19. Time dependence of the radial displacement remaining at the centre of three parabolic ice loads for viscosity models L1, L2 and L3. (a) is for the parabolic approximation to the Lake Bonneville load, (b) is for Fennoscandia, and (c) for Laurentide. On these semi-logarithmic plots the relaxation curves would be straight lines if the relaxation were perfectly exponential.

which will obtain in the limit of infinite time when the system has achieved isostatic equilibrium. This characteristic of the response is closely related to the free air gravity anomaly which we will discuss below, and the joint dependence upon the scale of the load and the viscosity model can be understood directly from the relaxation diagrams for the different viscosity models which were discussed previously. With reference to Fig. 19(a), for example, the characteristic angular order for the Lake Bonneville load is so high that only the M0 modes are excited for models L1 and L2 and only the L0 mode is excited for L3. The predicted response therefore decays almost exponentially (i.e. as a straight line on the semi-logarithmic plot in Fig. 19a). In Fig. 19(c), on the other hand, the dominant angular order for the Laurentide ice sheet is low and a spectrum of modes is excited. The decay curve for L1, for example, is at first dominated by the relatively short relaxation times of the M0 and C0 modes. After about 8 kyr, however, the M0 and C0 excitations have relaxed and the remaining history is dominated by the much longer relaxation times associated with the M1 and M2 modes. The decay is therefore strongly non-exponential, even though the viscosity of the L1 model is constant throughout the mantle. That realistic viscoelastic earth models may exhibit such behaviour is a point which is apparently not widely understood. This increase of apparent relaxation time with time is a characteristic of the response of this model which could easily be confused as being a direct indication of non-linear rheology. The response characteristics shown in Fig. 19(b) for Fennoscandia are intermediate between those of the smaller and larger scale loads.

5.2 FREE AIR GRAVITY RESPONSE AND THE EFFECT OF INITIAL ISOSTATIC DISEQUILIBRIUM

The free air gravity anomalies associated with such schematic loading events may be calculated as above, the sole difference being the use of Green's function (75) for the free air anomaly in place of that for radial displacement in equations (81) and (86). An example of one such calculation is shown in Fig. 20 for the model Laurentide load and viscoelastic model L1. Numerical data for the gravity anomaly at the centre of the Laurentide scale load calculated in this way for models L1 and L2 are listed in column 2 of Tables 10(a) and (b) respectively. These calculations are for the response to a parabolic ice sheet placed on the

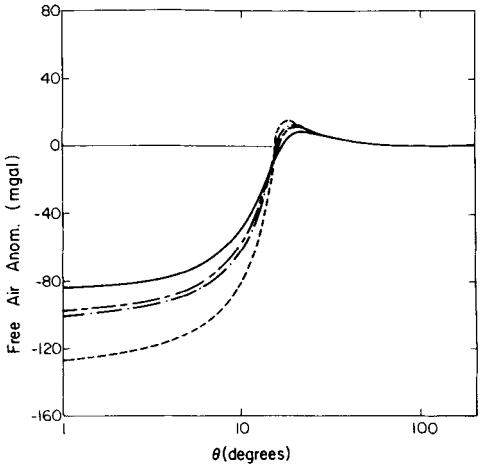

Figure 20. Same as Fig. 16 but for the free air gravity anomaly produced by a disc load of radius 15° on the surface of model L1.

Table 10. (a) Δg for Laurentide and viscosity model L1.

Time (kyr)	Δg: load added at $t = 0$	Δg: equilibrated load removed at $t = 0$	Δg: non-equilibrium load removed at $t = 0$
0	0	−127	−99
4	−84	−43	−29
8	−98	−29	−16
12	−100	−27	−14
16	−100	−27	−14
∞	−127	0	0

(b) Δg for Laurentide and viscosity model L2.

0	0	−127	−86
4	−33	−94	−65
8	−51	−76	−53
12	−63	−64	−43
16	−71	−56	−36
∞	−127	0	0

surface at $t = 0$ modified by subtraction of the infinite time response. The result of this calculation is a theoretical prediction of the uplift remaining and associated free air gravity anomaly which would exist had the ice sheet been in isostatic equilibrium with the underlying planet immediately prior to the unloading event. In order for this calculation to accord precisely with reality, the actual ice sheets would have to be resident on the Earth's surface for an infinite time prior to melting and this was certainly not the case. The oxygen isotopic data from deep sea sedimentary cores (Broecker & Van Donk 1970) discussed in Sabadini & Peltier (1981) has established that major continental ice sheet readvances have occurred on a time-scale of about 10^5 yr with the growth time-scale being very much longer than that for disintegration. In the remainder of this subsection we will employ the viscoelastic formalism to estimate the effects upon radial displacement and gravity anomaly which initial disequilibrium associated with such cyclic loading could have.

As we have seen previously, all of the viscoelastic impulse response Green's functions may be written in the form

$$G(\theta,t) = G^{\mathrm{E}}(\theta)\delta(t) + \sum_{n=0}^{\infty}\sum_{j=1}^{m} r_j^n \exp(-s_j^n t) P_n(\cos\theta) \tag{90}$$

where n is angular order, $1/s_j^n$ is the relaxation time for the jth mode and r_j^n the corresponding residue. If $L(\theta,t)$ is the load at location θ and time t then the response at time t is just

$$u(\theta,t) = \int_{-\infty}^{t} G(t-t') * L(t')dt'$$

where the $*$ denotes spatial convolution over the loaded surface. Suppose that at $t = 0$ the load at θ is $h_0(\theta)$ while for $t < 0$ the 'prehistory' of the loading event is $L_{\mathrm{p}}(\theta,t)$ and for $t > 0$ until the present the load is $h_0 + h(\theta,t)$, i.e.

$$\begin{aligned} L(\theta,t) &= L_{\mathrm{p}}(\theta,t) \quad \text{for} \quad t < 0 \\ &= h_0 + h(\theta,t) \quad \text{for} \quad t \geqslant 0 \end{aligned}$$

with $L_p(\theta,0) = h_0(\theta)$ and $h(\theta,0) \equiv 0$. For $t > 0$ we therefore have

$$u(\theta,t) = \int_{-\infty}^{0} G(t-t')*L_p(t')dt' + \int_0^t h_0*G(t-t')dt' + \int_0^t G(t-t')*h(t')dt' . \quad (91)$$

The second term on the rhs of (91) may be identified with the convolution of the Heaviside Green's function (74) over the loaded surface, i.e. $h_0*G^H(t)$ whereas the third term is the response to the deglaciation phase of the load cycle. This third term would be $-h_0*G^H(t)$ if all of the load were removed instantaneously.

The first term on the rhs of (91) is the response due to the prehistory $L_p(\theta,t)$. Making use of (90) it may be rewritten as

$$\int_{-\infty}^{0} G(t-t')*L_p(t')dt' = \sum_{n=0}^{\infty}\sum_{j=1}^{m} F_j^n(\theta)\frac{r_j^n}{s_j^n}\exp(-s_j^n t) \quad (92a)$$

where

$$F_j^n(\theta) = \int_{-\infty}^{0} P_n*L_p(t')s_j^n\exp(s_j^n t')dt' . \quad (92b)$$

This expression for $F_j^n(\theta)$ is greatly simplified if all sites have the same prehistory so that $L_p(\theta,t) = h_0(\theta)h_p(t)$ in which case the expression which replaces (92a) is

$$\int_{-\infty}^{0} G(t-t')*L_p(t')dt' = h_0*\sum_n\sum_j f_j^n\frac{r_j^n}{s_j^n}\exp(-s_j^n t)P_n \quad (93a)$$

where

$$f_j^n = \int_{-\infty}^{0} s_j^n\exp(s_j^n t')h_p(t')dt' . \quad (93b)$$

The functions f_j^n now contain all the information concerning the prehistory of loading. If the ice sheet had been left on the Earth's surface for an infinite time prior to melting so that the system was in isostatic equilibrium at $t = 0$ then $h_p(t) = H(t - t_\infty)$ where H is the Heaviside step function. With $t_\infty = -\infty$ it then follows from (93b) that $f_j^n = 1$. If the system were in isostatic equilibrium initially we would then have

$$\tilde{u}(t) = h_0*\sum_n\sum_j\frac{r_j^n}{s_j^n}\exp(-s_j^n t)P_n + h_0*G^H(t) + \int_0^t G(t-t')*h(t')dt' . \quad (94)$$

Using

$$G^H(\theta,t) = G^E(\theta) + \sum_n\sum_j\frac{r_j^n}{s_j^n}[1-\exp(-s_j^n t)]P_n$$

equation (94) can be written as

$$\tilde{u}(t) = h_0*\sum_n\sum_j\frac{r_j^n}{s_j^n}P_n + \int_0^t G(t-t')*h(t')dt'$$

or

$$\tilde{u}(t) = h_0*G^H(t=\infty) + \int_0^t G(t-t')*h(t')dt' . \quad (95)$$

Equation (95) shows that the isostatic response to the removal of a load $h_0(\theta)$ which is in equilibrium at $t = 0$ may be expressed as the sum of the infinite time (initial) response and the forced response. If the initially compensated load were removed instantaneously at $t = 0$ then from (95) the response for $t > 0$ would be

$$\tilde{u}(t) = h_0 * G^{\mathrm{H}}(t = \infty) - h_0 * G^{\mathrm{H}}(t). \tag{96}$$

If the melting of the Laurentide ice sheet could be approximated by the instantaneous removal of the previously discussed parabolic load then Fig. 19(c), which was constructed on the basis of (96), shows the way in which the depth of the initial depression would decrease as a function of time for each of the viscosity models L1, L2 and L3. The corresponding variation of the free air gravity anomaly with time for models L1 and L2 is shown in column 2 of Tables 10(a) and (b) respectively. The ICE1 melting chronology of Peltier & Andrews (1976) has the period of most rapid melting at 10–12 kyr BP. If we take the predicted gravity anomaly at 12 kyr as the prediction of the model for the present day, then it is quite clear from Table 10 that the model with high lower mantle viscosity (L2) must be rejected since it predicts a present-day free air anomaly of -64 mgal, which exceeds the observed anomaly of -30 to -40 mgal (Walcott 1970) by about a factor of 2. From column 2 of Table 10(a), however, we see that the uniform mantle viscosity model L1 fits this observation rather nicely if the assumption of initial isostatic equilibrium is valid and if the simple parabolic approximation to ICE1 is an adequate approximation to the history of unloading. The assumption of initial isostatic equilibrium cannot be strictly true, however, since the ice sheet did not reside on the Earth's surface for infinite time prior to its disintegration. How close the initial state actually was to equilibrium will depend upon the ratio of the residence time to the relaxation time.

We may directly assess the influence of initial isostatic disequilibrium as follows. Our general expression for the radial displacement response was (91–93)

$$u(t) = h_0 * \sum_{n=0}^{\infty} \sum_{j=1}^{m} f_j^n \frac{r_j^n}{s_j^n} \exp(-s_j^n t) P_n + h_0 * G^{\mathrm{H}}(t) + \int_0^t G(t - t') * h(t') dt' .$$

It therefore follows that the correction to the response $\tilde{u}(t)$ which would obtain if initial isostatic equilibrium had not prevailed is

$$u(t) - \tilde{u}(t) = -h_0 * E(t) \tag{97}$$

where the error (or correction) Green's function $E(\theta, t)$ is defined as

$$E(\theta, t) = \sum_{n=0}^{\infty} \sum_{j=1}^{m} (1 - f_j^n) \frac{r_j^n}{s_j^n} \exp(-s_j^n t) P_n(\cos\theta) . \tag{98}$$

From (97) it is clear that we may correct the prediction $\tilde{u}(t)$ for the effect of 'memory' of the previous loading history (prehistory) simply by subtracting from $\tilde{u}(t)$ a correction determined by convolving the load at $t = 0(h_0)$ with $E(\theta, t)$. To determine $E(\theta, t)$ from (98) we require the f_j^n defined in (93b) and these depend in turn upon the prehistory $h_{\mathrm{p}}(t)$. As we will argue in the following paragraphs it turns out that we can in fact construct a reasonable approximation to this prehistory on the basis of recently obtained isotopic information.

This information derives from the observed variability in the ratio of isotopic concentrations (O^{16}/O^{18}) of the stable isotopes of oxygen found as a function of depth in sedimentary cores taken in the major ocean basins (Fig. 21a). Although it was originally believed (Emiliani 1955) that this variability was a direct reflection of Pleistocene temperatures, it was subse-

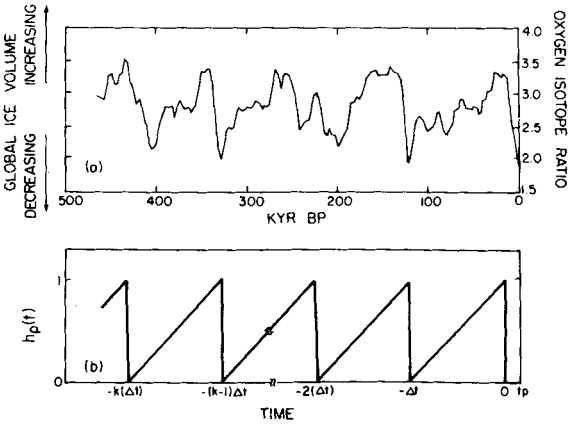

Figure 21. (a) Oxygen isotopic ratio as a function of time from a deep sea sedimentary core (Hays *et al.* 1976). (b) Time dependence of the loading history employed to construct the error Green's function employed to assess the effect upon the theoretical predictions of initial isostatic disequilibrium.

quently established (Imbrie & Kipp 1971) that the isotopic ratio reflected for the most part the variation of northern hemisphere ice volume. Broecker & van Donk (1970) were among the first to establish on the basis of these data that the northern hemisphere glacial-deglacial cycle is very nearly periodic with a time-scale of approximately 10^5 yr. Kukla *et al.* (1981) have most recently reviewed the signature of ice sheet growth and disintegration which is characteristic of each cycle. This signature, which is discussed in somewhat more detail in Hays, Imbrie & Shackleton (1976), is characterized by a very slow build-up of the major ice sheets over about 10^5 yr followed by an extremely rapid disintegration. This suggests that a good approximation to the prehistory is the sawtooth waveform shown in Fig. 21(b) and represented mathematically as

$$h_p(t) = \frac{(t + k\Delta t)}{\Delta t}, \quad -k\Delta t \leqslant t \leqslant -(k-1)\Delta t \tag{99}$$

with $\Delta t = 10^5$ yr the period characteristic of a single ice sheet advance. Substituting this expression in (93b) we find

$$f_j^n = \sum_{k=1}^{N} \int_{-k\Delta t}^{-(k-1)\Delta t} s_j^n \exp(s_j^n t') \frac{(t' + k\Delta t)}{\Delta t} dt'$$

where N is the number of cycles in the prehistory. Since the present glacial age has continued for about 2 million years, a time short compared to the continental drift time-scale of 10^8 yr on which significant changes of polar continentality might be expected to occur, yet long compared to the duration of a given glacial epoch (10^5 yr) we may safely assume $N \approx 20$ in computing the f_j^n. Direct evaluation of the above integral yields

$$f_j^n = \frac{\exp(-s_j^n \Delta t) - (1 - s_j^n \Delta t)}{s_j^n \Delta t} \cdot \left[\frac{1 - \exp(-N s_j^n \Delta t)}{1 - \exp(-s_j^n \Delta t)}\right]. \tag{100}$$

The ratio in the second bracketed term in (100) represents the effect on the f_j^n of the memory of the past N cycles. Note that if $s_j^n \Delta t$ is large, which is to say that characteristic

relaxation time is short compared to the build-up time of the ice sheet Δt, then $f_j^n \simeq 1$ and the mode (j,n) is very nearly in isostatic equilibrium at $t = 0$. If $s_j^n \Delta t \approx 1$ then $f_j^n \simeq 0.58$ provided $N > 2$, and the response in this mode would be just that for a reduced load $0.58 h_0(\theta)$ which was initially in equilibrium. If, however, $Ns_j^n \Delta t \ll 1$, then $f_j^n \simeq Ns_j^n \Delta t/2$ and by $t = 0$ the response is but a small fraction of what it would be in equilibrium.

In constructing the correction Green's function $E(\theta, t)$ we have calculated the f_j^n assuming $N = 30$, although for either viscosity model L1 or L2 the results are essentially unchanged for $N \gtrsim 20$. Free air gravity anomalies at the centre of the model Laurentide load, corrected in this way for initial isostatic disequilibrium, are listed in the last columns of Table 10(a) and (b) for models L1 and L2 respectively. For model L1 the correction is about 13 mgal while for L2 it is near 21 mgal. It is quite clear on the basis of these comparisons that the correction of the free air anomaly for the effect of initial disequilibrium may be extremely important and increases with the viscosity of the deep mantle. It has not been possible to quantify this idea previously because it had not been recognized that the oxygen isotope data provided accurate control on the time-scale of previous glaciation–deglaciation cycles.

A more detailed examination of the size of the correction as a function of the viscosity of the deep mantle is provided by Fig. 22 in which we plot the free air anomaly at $t = 12$ kyr as a function of the mantle viscosity beneath 670 km depth. The upper curve on this figure gives the free air anomaly under the assumption that isostatic equilibrium prevails initially, whereas the lower curve is the same prediction including the effect of isostatic disequilibrium at $t = 0$. Also shown on this diagram is the present-day observed anomaly of 30–40 mgal. Inspection of this figure shows that when isostatic equilibrium is assumed initially, the model with a constant mantle viscosity of 10^{22} P fits the observed free air anomaly very well. As the lower mantle viscosity is increased, however, the anomaly predicted for the present-day monotonically approaches an asymptotic value near 100 mgal which is near the maximum initial anomaly of 127 mgal. If the Laurentide ice sheet had been in equilibrium prior to

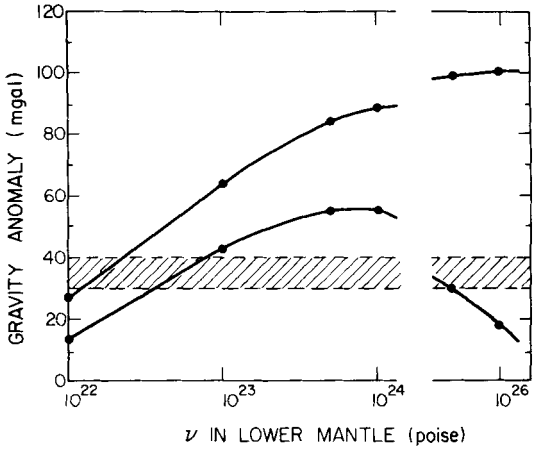

Figure 22. Plot of the present-day gravity anomaly in mgal at the centre of a disc load of Laurentide scale as a function of the viscosity in the lower mantle. The upper curve shows the anomaly which would obtain if initial isostatic equilibrium prevailed while the lower curve shows the effect of initial isostatic disequilibrium upon the predicted anomaly. Also shown by the horizontal hatched region is the anomaly observed over Hudson Bay today which is 30–40 mgal. The viscosity is given in units of poise and it should be noted that the effect of initial isostatic disequilibrium is to allow models with two different possible values for the lower mantle viscosity to fit the observed free air anomaly equally well.

disintegration then the Earth could not, therefore, have a lower mantle viscosity much in excess of that in the upper mantle. One would be hard pressed otherwise to explain the observed free air anomaly.

With a lower mantle viscosity even as high as 10^{23} P, however, characteristic relaxation times are no longer short compared to the time-scale of 10^5 yr which separates successive interglacials and the assumption of initial isostatic equilibrium is invalid. The lower curve in Fig. 22, which shows the predicted present-day free air anomaly corrected for initial disequilibrium, shows that in this case the anomaly is not a monotonically increasing function of the viscosity of the deep mantle. In this case the predicted anomaly agrees with the observed for either of two quite widely spaced values of the lower mantle viscosity. The first of these, $\nu_L^1 \simeq 5 \times 10^{22}$ P, is close to the value of 10^{22} P which fits the observed anomaly when initial equilibrium is assumed. The second root, $\nu_L^2 \simeq 5 \times 10^{25}$ P, is very much higher and exists as a possible solution because one may trade-off the degree of initial disequilibrium against the magnitude of the deep mantle viscosity. This analysis shows very clearly that a single observation of the free air anomaly associated with a specific deglaciation event provides an ambiguous datum in so far as its ability to constrain the viscosity of the deep mantle is concerned. It has not been possible previously to quantify the extent of this ambiguity because the value of the oxygen isotope data in this connection was apparently unrecognized. It is fortunate that the ambiguity may be removed by simultaneously constraining the mantle viscosity profile with relative sea-level data.

To appreciate the complementary nature of relative sea-level and free air gravity data we note that the former are effectively measurements of radial displacement with respect to a local zero since the heights of relict beaches are measured with respect to present-day local sea-level. These data therefore provide no information concerning the amount of uplift (submergence) which has yet to take place before isostatic equilibrium is restored. The free air gravity anomaly on the other hand, being an absolute measurement, provides a direct estimate of the degree of current disequilibrium. The two types of measurement are influenced, therefore, to a completely different extent by the degree of isostatic disequilibrium which exists prior to the onset of melting. This may be shown algebraically by using (97) to compute

$$u(t) - u(t_p) = \tilde{u}(t) - \tilde{u}(t_p) - h_0 * [E(t) - E(t_p)] \tag{101}$$

where t_p is used to denote the present time. The expression on the lhs of (101) is the radial displacement relative to that at $t = t_p$ which is just the quantity which is recorded (to a first approximation) in the relative sea-level data. The correction of the relative displacement for the effect of initial isostatic disequilibrium is given by the third term on the rhs of (101) in the form of a convolution of the initial load over a difference of error Green's functions. From (98), the expression in square brackets in (101) is just

$$E(t) - E(t_p) = \sum_{n=0}^{\infty} \sum_{j=1}^{m} (1 - f_j^n) \frac{r_j^n}{s_j^n} \exp(-s_j^n t) \{1 - \exp[-s_j^n (t_p - t)]\} P_n(\cos\theta). \tag{102}$$

Each term in the expansion for the difference Green function is therefore reduced by the factor $[1 - \exp(-s_j^n (t_p - t))]$ from the value which it has in the error Green's function itself and this factor is clearly zero when $t = t_p$. The size of the effect is illustrated by Fig. 23 in which we show relative displacement as a function of time at the centre of the model Laurentide load for viscosity models L1 and L2. For each viscosity model we compare the response curve computed on the basis of the assumption of initial equilibrium to that which includes the effect of the degree of initial disequilibrium implied by the particular viscosity

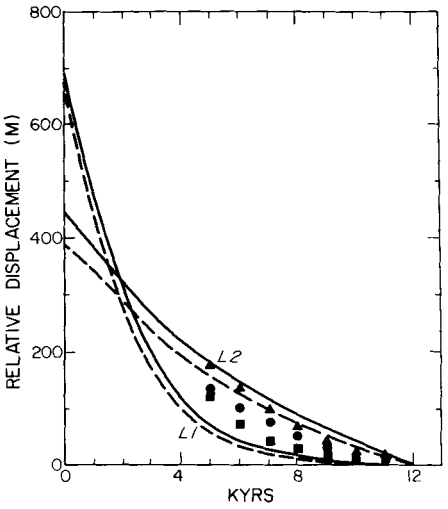

Figure 23. Time dependence of the relative displacement at the centre of the parabolic Laurentide scale load for viscosity models L1 and L2. The load is removed instantaneously at 12 kyr BP model time. Solid lines show the response obtained under the assumption of initial isostatic equilibrium while the dashed curves include the effects of isostatic disequilibrium estimated using the approximate prehistory shown in Fig. 21. Note that the effect of initial disequilibrium does not greatly affect the predicted relative displacement response. The solid rectangles, circles and triangles show the relative sea-level data points obtained by radiocarbon analysis of ancient beaches at Ottawa Islands, Churchill and Castle Island respectively. These sites are near what was the centre of the Laurentide ice sheet.

model. Inspection of this figure shows that the effect of initial disequilibrium (dashed curves) on the response for either viscosity model is very much smaller than the difference in response due to the difference in lower mantle viscosity in the models themselves. This is a very important result since it assures us that viscosity models rejected on the basis of RSL calculations done on the basis of the assumption of initial isostatic equilibrium cannot be brought back into contention by invoking initial isostatic disequilibrium. In Fig. 23 we have included data points from radiocarbon dated beaches on the Ottawa Islands in Hudson Bay, from Castle Island and from Churchill. To the extent that our model deglaciation history is an adequate approximation to the actual melting history it is then clear that the actual mantle viscosity profile should be intermediate between the L1 and L2 models. This is confirmed on the basis of the free air gravity data shown in Fig. 22 which require an increase of the lower mantle viscosity to a value near 5×10^{22} P. To make such tentative conclusions firmer than this requires the more thorough analysis of the complete RSL data set which is provided in Wu & Peltier (1982).

6 Conclusions

The analysis provided in the present paper has focused upon several fundamental properties of the global model of glacial isostatic adjustment which has been developed in previously cited papers which began with Peltier (1974). Those properties which have not received detailed discussion elsewhere include: (1) the effect of compressibility upon the Love number spectra and relaxation diagrams, (2) the importance of the lithosphere on the short-wavelength response, particularly in eliminating the non-geometric singularity at $\theta = 0$

in the infinite time response, and (3) the long relaxation time modes which are supported by the small density jumps in the mantle associated with solid–solid phase transitions.

The most important new result obtained in the present paper, however, concerned calculation of the small s asymptotes of the Love number spectra which are required to define the isostatic response of the viscoelastic earth model. The accurate calculation of these asymptotes was shown to be crucial to the calculation of the free air gravity signal associated with a particular deglaciation event. They were determined by solving a simple second-order ordinary differential equation to which the full spheroidal set of field equations reduces in the limit that the Laplace transform variable s tends to zero. This differential equation is in fact the same one which describes the quasi-static response in the fluid outer core, which should not be surprising since in the isostatic limit the entire Earth (with the exception of the lithosphere) is effectively inviscid.

Given an accurate method of calculating the isostatic response of the viscoelastic earth we have also been able to provide, for the first time, a quantitative assessment of the effects to be expected in consequence of deviations from isostatic equilibrium prior to ice sheet disintegration. We argued that oxygen isotopic data from deep sea sedimentary cores could be used to provide an accurate assessment, for a given viscosity model, of the degree of disequilibrium because they demonstrate quite conclusively: (1) that the time-scale between successive interglacials is $\approx 10^5$ yr, and (2) that the history of successive glaciations has a sawtooth form. Using this information we formulated the theory in such a way that predictions were made as the sum of the response which would be realized if initial equilibrium obtained and a correction (dependent upon the viscosity model) due to initial disequilibrium. The formulation was employed to demonstrate the characteristically different way in which relative sea-level and free air gravity data depend upon the degree of initial disequilibrium. This is of fundamental importance in understanding the 'quality' of the constraint upon the mantle viscosity profile which the free air signal provides.

References

Alterman, Z., Jarosch, H. & Pekeris, C. L., 1959. Oscillations of the Earth, *Proc. R. Soc. A*, **252**, 80–95.

Andrews, J. T., 1970. *A Geomorphological Study of Postglacial Uplift with Particular Reference to Arctic Canada*, Oxford, 156 pp.

Backus, G. E., 1967. Converting vector and tensor equations to scalar equations in spherical coordinates, *Geophys. J. R. astr. Soc.*, **13**, 71.

Backus, G. E. & Gilbert, J. F., 1967. Numerical applications of a formalism for geophysical inverse problems, *Geophys. J. R. astr. Soc.*, **13**, 247–276.

Berckhemer, H., Auer, F. & Drisler, J., 1979. High temperature anelasticity and elasticity of mantle peridotites, *Phys. Earth planet. Int.*, **20**, 48–59.

Broecker, W. S. & Van Donk, J., 1970. Insolation changes, ice volumes, and the O^{18} record in deep-sea cores, *Rev. Geophys. Space Phys.*, **8**, 169–198.

Cathles, L. M., 1975. *The Viscosity of the Earth's Mantle*, Princeton University Press, New Jersey.

Chinnery, M. A., 1975. The static deformation of an earth with a fluid core: a physical approach, *Geophys. J. R. astr. Soc.*, **42**, 461.

Clark, J. A., Farrell, W. E. & Peltier, W. R., 1978. Global changes in postglacial sea level: a numerical calculation, *Quat. Res.*, **9**, 265–287.

Crittenden, M. D. Jr, 1963. Effective viscosity of the Earth derived from isostatic loading of Pleistocene Lake Bonneville, *J. geophys. Res.*, **68**, 5517.

Crossley, D. J. & Gubbins, D., 1975. Static deformation of the Earth's liquid core, *Geophys. Res. Lett.*, **2**, 1.

Dahlen, F. A. & Fels, S. B., 1978. A physical explanation of the static core paradox, *Geophys. J. R. astr. Soc.*, **55**, 317–332.

Emiliani, C., 1955. Pleistocene temperatures, *J. Geol.*, **63**, 538.

Farrell, W. E., 1972. Deformation of the Earth by surface loads, *Rev. Geophys. Space Phys.*, **10**, 761.

Gilbert, F. & Backus, G., 1968. Elastic-gravitational vibrations of a radially stratified sphere, in *Dynamics of Stratified Solids*, p. 82, ed. Herrmann, G., American Society of Mechanical Engineers, New York.

Gilbert, F. & Dziewonski, A., 1975. An application of normal mode theory to the retrieval of structural parameters and source mechanisms from seismic spectra, *Phil. Trans. R. Soc. A*, **278**, 187.

Haskell, N. A., 1935. The motion of a viscous fluid under a surface load 1, *Physics*, **6**(8), 265.

Haskell, N. A., 1936. The motion of a viscous fluid under a surface load 2, *Physics*, **7**(2), 56.

Hays, J. D., Imbrie, J. & Shackleton, N. J., 1976. Variations in the Earth's orbit: pacemaker of the ice ages, *Science*, **194**, 1121.

Hobson, E. W., 1955. *The Theory of Spherical and Ellipsoidal Harmonics*, Chelsea, New York.

Imbrie, J. & Kipp, N. G., 1971. A new micropaleontological method for quantitative paleoclimatology: application to a late Pleistocene Caribbean core, in *Late Cenozoic Glacial Ages*, ed. Turekian, K. K., Yale University Press, New Haven.

Jackson, J. D., 1962. *Classical Electrodynamics*, Wiley, New York.

Kohlstedt, D. L. & Goetze, C., 1974. Low-stress and high temperature creep in olivine single crystals, *J. geophys. Res.*, **79**, 2045–2051.

Kukla, G., Berger, A., Lotti, R. & Brown, J., 1981. Orbital signature of interglacials, *Nature*, **290**, 295.

Lentz, W. J., 1976. Generating Bessel functions in Mie scattering calculations using continued fractions, *Appl. Opt.*, **15**, 668–671.

Longman, I. M., 1963. A Green's function for determining the deformation of the earth under surface mass loads, 2, Computations and numerical results, *J. geophys. Res.*, **68**, 485.

Love, A. E. H., 1911. *Some Problems of Geodynamics*, Dover, New York.

Love, A. E. H., 1927. *A Treatise on the Mathematical Theory of Elasticity*, 4th edn, Dover, New York.

McConnell, R. K. Jr, 1965. Isostatic adjustment in a layered earth, *J. geophys. Res.*, **70**, 5171.

McConnell, R. K. Jr, 1968. Viscosity of the mantle from relaxation time spectra of isostatic adjustment, *J. geophys. Res.*, **73**, 7089.

Munk, W. H. & MacDonald, G. J. F., 1960. *The Rotation of the Earth*, Cambridge Univeristy Press.

Parsons, B. E., 1972. Changes in the Earth's shape, *PhD thesis*, Cambridge University.

Peltier, W. R., 1974. The impulse response of a Maxwell Earth, *Rev. Geophys. Space Phys.*, **12**, 649.

Peltier, W. R., 1976. Glacial-isostatic adjustment – II. The inverse problem, *Geophys. J. R. astr. Soc.*, **46**, 669.

Peltier, W. R., 1980. Mantle convection and viscosity, in *Physics of the Earth's Interior*, eds Dziewonski, A. M. & Boschi, E., North Holland, New York.

Peltier, W. R., 1981. Ice age geodynamics, *A. Rev. Earth planet. Sci.*, **9**, 199–225.

Peltier, W. R. & Andrews, J. T., 1976. Glacial-isostatic adjustment – I. The forward problem, *Geophys. J. R. astr. Soc.*, **46**, 605.

Peltier, W. R., Farrell, W. E. & Clark, J. A., 1978. Glacial isostasy and relative sea level: a global finite element model, *Tectonophys.*, **50**, 81–110.

Peltier, W. R., Wu, P. & Yuen, D. A., 1981. The viscosities of the Earth's mantle, in *Anelasticity in the Earth*, eds Stacey, F. D., Nicholas, A. & Paterson, M. S., Geodynamics Series Volume 4, American Geophysical Union, Washington, DC.

Sabadini, R. & Peltier, W. R., 1981. Pleistocene deglaciation and the Earth's rotation: implications for mantle viscosity, *Geophys. J. R. astr. Soc.*, **66**, 553–578.

Smylie, D. E. & Mansinha, L., 1971. The elasticity theory of dislocations in real earth models and changes in the rotation of the Earth, *Geophys. J. R. astr. Soc.*, **23**, 329.

Twiss, R. J., 1976. Structural superplastic creep and linear viscosity in the Earth's mantle, *Earth planet. Sci. Lett.*, **33**, 86–100.

Walcott, R. I., 1970. Isostatic response to loading of the crust in Canada, *Can. J. Earth Sci.*, **7**, 716–727.

Walcott, R. I., 1980. Rheological models and observational data of glacio-isostatic rebound, in *Earth Rheology, Isostasy and Eustasy*, ed. Mörner, N. A., Wiley, London.

Wu, P. & Peltier, W. R., 1982. The free air gravity anomaly as a constraint upon deep mantle viscosity, *Geophys. J. R. astr. Soc.*, submitted.